

# The Variation of Ionospheric O+ and H+ Outflow on Storm Timescales

Niloufar Nowrouzi<sup>1</sup>, Lynn M. Kistler<sup>2</sup>, Kai Zhao<sup>3</sup>, Eric J Lund<sup>4</sup>, Christopher G. Mouikis<sup>2</sup>, Genevieve Payne<sup>5</sup>, and Berndt Klecker<sup>6</sup>

<sup>1</sup>Center for Space Physics Boston University

<sup>2</sup>University of New Hampshire

<sup>3</sup>Nanjing University of Information Science and Technology

<sup>4</sup>College Brook Scientific

<sup>5</sup>Colorado Boulder

<sup>6</sup>MPI

August 4, 2023

## Abstract

Geomagnetic storms are primarily driven by stream interaction regions (SIRs) and coronal mass ejections (CMEs). Since SIR and CME storms have different solar wind and magnetic field characteristics, the magnetospheric response may vary accordingly. Using FAST/TEAMS data, we investigate the variation of ionospheric O+ and H+ outflow as a function of geomagnetic storm phase during SIR and CME magnetic storms. The effects of storm size and solar EUV flux, including solar cycle and seasonal effects, on storm time ionospheric outflow, are also investigated. The results show that for both CME and SIR storms, the O+ and H+ fluence peaks during the main phase, and then declines in the recovery phase. However, for CME storms, there is also significant increase during the initial phase. Because the outflow starts during the initial phase in CME storms, there is time for the O+ to reach the plasma sheet before the start of the main phase. Since plasma is convected into the ring current from the plasma sheet during the main phase, this may explain why more O+ is observed in the ring current during CME storms than during SIR storms. We also find that outflow fluence is higher for large storms than moderate storms and is higher during solar maximum than solar minimum.

## Hosted file

966200\_0\_art\_file\_11098015\_rwck37.docx available at <https://authorea.com/users/631351/articles/650634-the-variation-of-ionospheric-o-and-h-outflow-on-storm-timescales>

## Hosted file

966200\_0\_table\_11096271\_rwbs9t.docx available at <https://authorea.com/users/631351/articles/650634-the-variation-of-ionospheric-o-and-h-outflow-on-storm-timescales>

## Hosted file

966200\_0\_table\_11096272\_rwbs9t.docx available at <https://authorea.com/users/631351/articles/650634-the-variation-of-ionospheric-o-and-h-outflow-on-storm-timescales>

# The Variation of Ionospheric O<sup>+</sup> and H<sup>+</sup> Outflow on Storm Timescales

N. Nowrouzi<sup>1,2,†</sup>, L. M. Kistler<sup>1,2</sup>, K Zhao<sup>3</sup>, E. J. Lund<sup>1</sup>, C. Mouikis<sup>1</sup>, G. Payne<sup>4</sup>, B. Klecker<sup>5</sup>

<sup>1</sup>Space Science Center, University of New Hampshire, Durham, NH, USA.

<sup>2</sup>Physics Department, University of New Hampshire, Durham, NH, USA.

<sup>3</sup>School of Mathematics and Statistics, Nanjing University of Information Science and Technology, Nanjing, China.

<sup>4</sup>University of Colorado Boulder.

<sup>5</sup>Max-Planck-Institut für extraterrestrische Physik, Garching, Germany.

Corresponding author: Niloufar Nowrouzi (nowrouzi@bu.edu)

†Now at Boston University.

## Key Points:

- Both CME and SIR storms have their maximum O<sup>+</sup> and H<sup>+</sup> outflow during the main phase, and a decrease during the recovery phase.
- During CME storms, the outflow increases during the initial phase, while during SIR storms, it doesn't increase until the main phase.
- This difference in outflow timing may explain why more O<sup>+</sup> is observed in the ring current during CME storms than during SIR storms.

## Abstract

Geomagnetic storms are primarily driven by stream interaction regions (SIRs) and coronal mass ejections (CMEs). Since SIR and CME storms have different solar wind and magnetic field characteristics, the magnetospheric response may vary accordingly. Using FAST/TEAMS data, we investigate the variation of ionospheric O<sup>+</sup> and H<sup>+</sup> outflow as a function of geomagnetic storm phase during SIR and CME magnetic storms. The effects of storm size and solar EUV flux, including solar cycle and seasonal effects, on storm time ionospheric outflow,

27 are also investigated. The results show that for both CME and SIR storms, the  $O^+$  and  $H^+$  fluence  
28 peaks during the main phase, and then declines in the recovery phase. However, for CME  
29 storms, there is also significant increase during the initial phase. Because the outflow starts  
30 during the initial phase in CME storms, there is time for the  $O^+$  to reach the plasma sheet before  
31 the start of the main phase. Since plasma is convected into the ring current from the plasma  
32 sheet during the main phase, this may explain why more  $O^+$  is observed in the ring current during  
33 CME storms than during SIR storms. We also find that outflow fluence is higher for large  
34 storms than moderate storms and is higher during solar maximum than solar minimum.

35

## 36 **1 Introduction**

37         There are two sources for the magnetospheric plasma: the solar wind and the ionosphere  
38 (Sharp, Johnson, & Shelley, 1974; Shelley et al., 1972). The solar wind consists predominantly  
39 of  $H^+$  ions, with  $\sim 4\%$   $He^{++}$  ions and  $<1\%$  other species. The ionospheric contribution mainly  
40 consists of  $H^+$ , the  $O^+$  and  $N^+$  group (indistinguishable in some instruments, and called  $O^+$  in this  
41 paper) and  $He^+$ . Because  $H^+$  can come from both sources,  $O^+$  is often used as the tracer of  
42 ionospheric plasma. In addition, because of its higher mass and larger gyroradius, increased  $O^+$   
43 abundance can change the magnetospheric dynamics. The ionospheric outflow comes  
44 predominantly from the auroral oval, from the dayside cusp region around to the nightside  
45 auroral region. From the auroral regions, the ionospheric plasma is transported throughout the  
46 magnetosphere. The dayside outflow flows over the polar cap into the lobe, and can then enter  
47 the plasma sheet through reconnection. The nightside outflow has direct access to the near-earth  
48 plasma sheet. During geomagnetic storms, the plasma in the near-earth plasma sheet is driven  
49 into the inner magnetosphere by enhanced convection, where it forms the storm-time ring  
50 current.

51         Many previous studies have shown that the contribution of the ionospheric heavy ions to  
52 the magnetosphere tends to increase with geomagnetic activity at all locations along the transport  
53 path. During disturbed geomagnetic conditions, as identified by Kp and Dst indexes, the  
54 strength of ion outflow increases compared to quiet times, and the composition of ion outflow  
55 changes, with  $H^+$  being dominant during quiet times and  $O^+$  being dominant during active or  
56 storm times (Collin et al., 1984; Cully et al., 2003; Wilson et al., 2004; Yau et al., 1988). (Liao et

57 al. (2010) showed that the occurrence of  $O^+$  beams in the polar caps and lobes, identified as the  
58 cusp-origin outflow, increases during geomagnetic storms. During storms, these ions enter the  
59 plasma sheet for many hours (Kistler et al., 2010). Young et al. (1982), Mouikis et al. (2010),  
60 and Maggiolo & Kistler (2014) have shown that the  $O^+$  density in the plasma sheet increases  
61 with  $K_p$ .

62 For the ring current, Hamilton et al. (1988) and Greenspan & Hamilton, (2002) showed  
63 that the ionospheric heavy ion contribution to the ring current goes up during the main phase of a  
64 geomagnetic storm. Mouikis et al. (2019) separated geomagnetic storms into Coronal Mass  
65 Ejection (CME) driven storms and Stream Interaction Region (SIR) driven storms, and  
66 performed a superposed epoch analysis of the ring current  $O^+$  and  $H^+$  pressure as a function of  
67 geomagnetic storm phases. They reported a larger enhancement of the  $O^+$  pressure, that is  
68 contributed mostly by the low-energy ions  $< \sim 55$  keV, during the main phase in CME storms  
69 than in SIR storms, while for the  $H^+$  pressure, there is almost no significant difference between  
70 CME and SIR storms.

71 Outside of the ring current, while the general correlation with magnetic activity is  
72 established, the timing of the increased outflow relative to the phases of the storm has not been  
73 shown. The timing is critical because the  $O^+$  outflow is relatively slow moving. For ionospheric  
74 ions to convect into the ring current during a storm main phase, they need to first travel to the  
75 near-earth plasma sheet.  $O^+$  outflow from the cusp would take at least 2 hours (Kistler et al.,  
76 2019) to reach the plasma sheet. Nightside outflow will reach the nightside plasma sheet more  
77 quickly, but tends to be at lower energies, and so may not contribute significantly to the particle  
78 pressure that forms the ring current (Kistler et al., 2019). So, it remains an open question how  
79 the ionospheric ions are able to populate the pre-storm or main phase near-earth plasma sheet  
80 and get heated in time to be injected into the ring current during storm main phase.

81 To investigate this problem, this study uses a superposed epoch analysis of FAST data to  
82 examine how the ion outflow varies during a storm, addressing the differences between the two  
83 main drivers of geomagnetic storms, CMEs and SIRs. These two solar wind structures, on  
84 average have different solar wind and IMF characteristics when they impact the earth (Tsurutani  
85 et al., 2006). During the initial phase, CMEs often have an abrupt increase in ram pressure due  
86 to fast forward shocks. SIRs are usually not preceded by a shock at 1 AU, and have more

87 gradual onsets. CME structures often contain long-lasting southward IMF Bz. SIR structures  
88 usually have shorter excursions of southward IMF Bz, less sustained than for a CME. Because  
89 the CME and SIR solar wind structures and the amount of transported energy are different  
90 (Borovsky & Denton, 2006), it is likely that the ionospheric outflow driven by the structures will  
91 be different. The differences found by Mouikis et al. (2019) in the ring current may be due to  
92 differences in outflow fluence, or differences in outflow timing. Thus, for our study, we  
93 compare storms with the two drivers to identify the differences.

94 In addition to the storm drivers, the solar EUV flux may impact the outflow as well.  
95 Globally, solar EUV changes with the solar cycle, and locally, the incident EUV flux changes  
96 with the season. Yau, Beckwith et al. (1985), using DE-1 data, and Cully et al. (2003), using  
97 Akebono, showed that the occurrence of upflowing  $O^+$  increased with F10.7, the proxy for Solar  
98 EUV, with a much smaller increase for  $H^+$ . The results for seasonal dependence are more mixed.  
99 Yau, Beckwith et al. (1985) observed that the  $O^+$  outflow increased towards summer solstice.  
100 Peterson et al. (2006), on the other hand, using POLAR/TIMAS, found no systematic change in  
101  $O^+$  or  $H^+$  outflow flux with season, although  $He^+$  had a strong seasonal dependence. Collin et al.  
102 (1998) found a strong seasonal variation in the occurrence of upflowing beams, with more beams  
103 observed in the 1800-24:00 MLT sector during winter, but saw no change in the distribution of  
104 conics, and so the overall impact on outflow fluence may not be large. While solar EUV and  
105 season likely don't change the outflow on storm time-scales, they will impact the total fluence  
106 observed. Thus, we have also compared the outflow response of storms that occur during  
107 different phases of the solar cycle and under different seasons so that outflow rates under  
108 different conditions can be compared with other studies.

## 109 **2 Instrumentation**

110 To better understand auroral acceleration physics and magnetosphere-ionosphere  
111 coupling, the FAST satellite was launched in August 1996 into an elliptical polar orbit with a  
112 period of 133 minutes, an inclination angle of  $83^\circ$ , perigee of  $\sim 350$  km, and apogee of  $\sim 4175$  km  
113 (Charles W. Carlson, 1998). The FAST payload consists of six scientific instruments; the  
114 ElectroStatic Analyzers (ESAs) for gathering the electron (EESA) and ion (IESA) energy and  
115 pitch angle distributions (C W Carlson et al., 2001) the Time-of-flight Energy Angle Mass  
116 Spectrograph (TEAMS) instrument (Klumpar et al., 2001) to measure the 3-D distribution

117 functions of particle species  $H^+$ ,  $O^+$ ,  $He^+$  and  $He^{++}$ , the Electric Field Sensors (Ergun et al., 2001)  
118 and the Magnetic Field Experiment sensors (Elphic et al., 2001) to measure the electric and  
119 magnetic fields data, respectively, and the Instrument Data Processor Unit (IDPU) to perform  
120 data processing.

121 In this paper, we use the recently released TEAMS L2 data to measure the ionospheric  
122 outflow and investigate the variation of ionospheric  $O^+$  and  $H^+$  outflow flux on storm  
123 timescales. The TEAMS L2 dataset includes a recalibration and a number of corrections. Over  
124 time, the TEAMS MCP efficiency degraded, with the amount of degradation depending on the  
125 position of the instrument positions (angular bins). In particular, the equatorial bins had very  
126 low efficiency. Using observations of plasma regions where assuming plasma gyrotropy is valid,  
127 the efficiencies of the individual positions were recalibrated using methods described in Kistler  
128 et al. (2013). Subsequently, a final cross-calibration with the IESA data set was performed that  
129 adjusted the overall level. A deadtime correction was also introduced that uses the IESA data,  
130 which is much less susceptible to deadtime, to determine the total count rate in the TEAMS  
131 instrument and applies a deadtime correction based on the count rate. The TEAMS measurement  
132 is corrected for spacecraft potential by shifting the distribution function, assuming the spacecraft  
133 charging is uniform around the spacecraft, and then the data is transformed to the convection  
134 frame ( $ExB$  frame) and sorted into pitch angle. Time periods when the spacecraft potential is  
135 less than  $-6V$  are excluded. Finally, time periods with incomplete data packets are flagged and  
136 excluded from the analysis.

### 137 **3 Data Selection**

#### 138 3.1 Geomagnetic storms

139 To identify and characterize the storms, we used the Disturbance Storm-Time (Dst)  
140 index, upstream parameters including the  $z$  component of interplanetary magnetic field ( $IMF$   
141  $B_z$ ), the solar wind pressure ( $P_{SW}$ ), the solar wind density ( $n_{SW}$ ), the solar wind speed ( $V_{SW}$ ), and  
142 the geomagnetic and solar activity indices Auroral Electrojet ( $AE$ ), the  $Kp$  index (multiplied by  
143 10) and the F10.7 index. A sample plot of these parameters for the storm of May 15, 2005 is  
144 presented in Figure 1.

145           The storm phases were identified using the Dst index. We identified four critical times  
146 for each storm. Some storms have an initial phase that starts when the Dst rises sharply. This is  
147 usually caused by an increase in solar wind dynamic pressure. The vertical orange line indicates  
148 the increase time in Figure 1; this feature is not observable in all storms. The time when the Dst  
149 starts to drop is called the storm onset time and is shown with a vertical green line in Figure 1.  
150 The initial phase is the time between the Dst increase and the onset time. After onset, Dst  
151 decreases until it reaches the minimum value of Dst, shown with a red vertical line. The interval  
152 between onset and Dst minimum is called the main phase. IMF Bz is generally negative  
153 (southward) during this time. At the peak of the storm, the IMF Bz usually turns positive  
154 (northward). After the main phase, Dst increases back to zero in the recovery phase. For our  
155 study, we have included the time from Dst minimum to the time when the Dst index passes  
156  $\frac{1}{3} \times Dst_{minimum}$  or -20 nT, whichever is earlier, for the recovery phase. The vertical blue line  
157 shows the end of the recovery phase for this storm. In addition to these three storm phases, we  
158 defined a prestorm phase that extends from 24 hours before the initial phase to the initial phase.  
159 If there is no initial phase, the prestorm phase starts 27 hours before the onset and ends at the  
160 onset. In some cases, there are storms in close succession, such that the prestorm of the second  
161 storm overlaps with the first storm's recovery phase. To avoid double-counting data from the  
162 recovery phase in the prestorm phase, we added the condition that the Kp index must be less than  
163 3 during the prestorm phase. With these definitions, we compiled a list of all geomagnetic storms  
164 that showed the classic storm profile (ie. a clear main phase and recovery phase) from solar cycle  
165 23, from 1996 to 2009, that showed the classic storm profile (ie. a clear main phase and recovery  
166 phase). Storms with more complicated storm profiles, for which clear main and recovery phases  
167 could not be identified, were excluded. The minimum Dst index for the storms on the list is less  
168 than -50 nT.

169           We then identified the storm driver, CME or SIR, for each of these storms using  
170 previously published catalogs (Jian et al., 2006b, 2006a; Matamba & Habarulema, 2018;  
171 Richardson & Cane, 2010) and only used the storms with one identified driver in the study.

172           In Figure 2, the top panel shows the smoothed daily averaged F10.7 for solar cycle 23  
173 and the bottom panel shows  $Dst_{minimum}$  values for all identified storms used in the study. The  
174 red and blue symbols present the SIR and CME driven storms, respectively. As discussed in the

175 introduction, in addition to the solar wind driving conditions, the outflow flux also varies with  
176 solar EUV and possibly with solar illumination, represented by the season. Therefore, we  
177 divided the solar cycle into a solar minimum and a solar maximum phase using the F10.7 index  
178 of 150 (s.f.u) as the boundary. The minimum phase includes two sub-phases: descending and  
179 ascending phases. In Figure 2, the dotted vertical lines separate the solar cycle phases.

180 The FAST spacecraft data collection alternated between using northern hemisphere and  
181 southern hemisphere passes, and only rarely used both in the same orbit, so most storms include  
182 data from either the north or from the south. For data from the northern hemisphere, the summer  
183 season is from 03-22/00:00 to 09-22/00:00, and the winter season is from 09-22/00:00 to 03-  
184 22/00:00. For southern hemisphere data, the seasons are switched. The storms with TEAMS data  
185 from summer season are shown with triangles and from winter season with squares.

186 In Figure 2, the scatter plot of  $Dst_{minimum}$  shows that the most intense storms occurred  
187 during the solar maximum phase and the first years of the declining phase. To study the effect of  
188 storm intensity on the ionospheric outflow, we divided the storms into two groups: moderate  
189 storms with  $-150 nT \leq Dst_{minimum} < -50 nT$  and intense storm with  $-150 nT \geq$   
190  $Dst_{minimum}$ . The horizontal dashed line in the bottom panel of Figure 2 indicates the separation  
191 of moderate and intense storms.

192 In Table 1. we list the total number of storms used in this analysis for each driver that fall  
193 into each category.

### 194 3.2 Ionospheric outflow flux

195 Equation 1 is used to calculate the ion outflow flux. In this equation, the variables  $\alpha$ ,  $E$ ,  
196 and  $j(m, E, \alpha)$  represent the pitch angle, energy, and energy flux data, respectively.

$$197 \quad \Phi(m) = 2\pi \int_{E=10eV}^{E_{cutoff}} \int j(m, E, \alpha) |\sin(\alpha) \sin(\Delta\alpha) \cos(\alpha) \cos(\Delta\alpha)| dE d\alpha \quad \text{Equation 1}$$

198 For the energy integration, a lower energy threshold of 10 eV and a dynamic upper  
199 energy cutoff is used. The upper cutoff prevents the contribution of the magnetospheric  
200 precipitation population in the outflow flux calculation (Hatch et al., 2020; Zhao et al., 2020). To  
201 calculate the dynamic cutoff energy, we used the ratio of the upward ( $90^\circ < pa < 180^\circ$ ) and  
202 downward ( $270^\circ < pa < 360^\circ$ ) flux from the iESA data at each energy for the northern

203 hemisphere. At any time, the cutoff energy is the highest energy with ratio  $\left(\frac{flux_{upward}}{flux_{downward}}\right)$  bigger  
204 than 2. If, at time  $t$ , the ratio never is bigger than 2, the cutoff energy is set to the minimum  
205 value, 10 eV, so there is no contribution to the flux. For this time, the eflux value corresponding  
206 to one count along the magnetic field direction is recorded.

207 A TEAMS summary plot of FAST orbit 8277, passing the noon-midnight of the northern  
208 hemisphere during the main storm phase, is shown in Figure 3. Panels (a), (b), and (c) contain  
209 the  $H^+$  energy spectrogram, the  $H^+$  pitch angle spectrogram plots for energies  $< 1$  keV and the  $H^+$   
210 pitch angle spectrogram for energies  $> 1$  keV, respectively. Panels (d), (e), and (f) present the  
211 corresponding spectrograms for  $O^+$ . Panel (g) shows the spacecraft's potential.

212 The black lines in panels (h) and (i) give the in-situ outflow flux for  $H^+$  and  $O^+$  species,  
213 which are calculated from Equation 1.

214 We normalize the net flux by mapping it to 300 km. The net outflow flux is inversely  
215 proportional to the cross-section of the flux tube,  $\Phi \propto \frac{1}{A}$ . On the other hand, the cross-section of  
216 the flux tube is inversely proportional to the magnitude of the magnetic field,  $A \propto \frac{1}{B}$ . At these  
217 altitudes, a dipole magnetic field is adequate for the mapping. The dipole magnetic field is  
218 inversely proportional to the third power of altitude,  $B \propto \frac{1}{r^3}$ . So, the net outflow flux is inversely  
219 proportional to the third power of altitude,  $\Phi \propto \frac{1}{r^3}$ .

220 The normalized net outflow flux, which we call outflow flux from now on, is plotted with  
221 the red line in panels (h) for  $H^+$  and (i) for  $O^+$ . Also, the  $H^+$  and  $O^+$  outflow flux is plotted along  
222 the FAST trajectory in the dial plots located on the right side of panels (h) and (i) in Figure 3.

223 To determine how the outflow varies with the storm phase, we present the averaged  
224 outflow flux of  $H^+$  and  $O^+$  binned by MLT-ILAT. Only data above 1500 km altitude are  
225 included. Figure 4. shows an example of the data display we will use, in this case for  $O^+$  during  
226 CME storms.

227 We divide the normalized net outflow flux by storm phase: prestorm, initial phase, main  
228 phase, and recovery phase (four columns). Four rows are shown: trajectory, all storms, moderate,  
229 and intense. The trajectory row shows the  $O^+$  outflow flux along the spacecraft trajectory for  
230 each storm phase. The data is limited to Invariant Latitude (ILAT) greater than  $50^\circ$ ; the circles

231 shown are in  $10^\circ$  increments. The next row shows all the storm data binned into 40 ILAT bins  
232 with a width of  $1^\circ$  and 24 magnetic local time (MLT) bins with a time width of 1 hour. The  $O^+$   
233 outflow flux measurements in each MLT-ILAT bin are averaged, and the averaged flux is  
234 assigned to the bin. The big circular plots show the averaged flux for each species. The smaller  
235 circular plots above each big plot show the number of data points associated with averaged flux  
236 of each MLT-ILAT bin in the smaller circular plots above the big plot. The third and fourth rows  
237 show the binned and averaged flux separately for the moderate and intense storms. Subsequently,  
238 we use these data to calculate the total fluence in four local time sectors.

## 239 **4 Storm phases and storm intensity**

### 240 **4.1 $O^+$ outflow flux**

241 Figure 4 shows the  $O^+$  outflow data for CME storms. There is good coverage for all  
242 phases, with the highest number of data points for the recovery and prestorm phases. Because of  
243 the short duration of the storm initial phase, there are fewer data points from the initial phase.  
244 The all-storm panel shows that before the storm, there is a region of weak outflow in the cusp  
245 region, between  $\sim 70^\circ$  and  $85^\circ$  invariant latitude and extending from 15MLT to 6 MLT. In the  
246 nightside sector, the weak outflow is also observed between  $70^\circ$  and  $80^\circ$  invariant latitudes.  
247 During the initial phase, the intensity of outflow flux increases and expands in both MLT and  
248 ILAT. The cusp shows the highest outflow, extending from 9 MLT to 17 MLT, with high  
249 outflow fluxes observed down to  $67^\circ$ . From 7 MLT to 9 MLT, the outflow reaches the lower  
250 latitude of  $63^\circ$ . The outflow flux on the nightside also increases, covering the latitude between  
251  $75^\circ$  and  $80^\circ$ . During the main phase, the outflow flux increases significantly and is observed in  
252 all MLT regions. The coverage of high flux is between  $60^\circ$  and  $80^\circ$  invariant latitudes for  
253 dawnside and dayside and between  $75^\circ$  and  $60^\circ$  for duskside and nightside. In the recovery  
254 phase, the outflow flux decreases, with MLT-ILAT coverage similar to the main phase.

255 The next two rows compare the outflow from moderate and intense storms. As shown in  
256 Figure 2, we expect to have better statistics for moderate storms than intense storms. Comparing  
257 the  $O^+$  outflow flux during moderate and intense storms shows that although the variation and  
258 spatial distribution of ionospheric  $O^+$  outflow during storm phases are similar for both storm

259 intensity groups, intense storms drive higher O<sup>+</sup> outflow. The intense outflow is also  
 260 occasionally observed down to 50° latitude.

261 Figure 5 shows the averaged O<sup>+</sup> outflow flux before and during the phases of SIR storms.  
 262 In general, there are fewer SIR storms, therefore the MLT-ILAT coverage is not as good. From  
 263 Table 1. we only have one intense SIR storm, so we limit our epoch analysis study to moderate  
 264 SIR storms. Like the prestorm phase in CME storms, there is O<sup>+</sup> outflow flux before the storm,  
 265 primarily at noon and after midnight. However, unlike the initial phase of CME storms, the flux  
 266 does not increase significantly during the initial phase of SIR storms. Like CME storms, the  
 267 maximum outflow flux occurs during the main phase and is observed in all MLT sectors. A  
 268 distinct difference is that for or SIR's the maximum outflow is on the dawn side. The outflow  
 269 does not generally extend as low in ILAT for SIR storms. In the recovery phase, the outflow flux  
 270 declines, and the distribution is quite similar to the recovery phase of moderate CME storms.

271 The ion outflow rate (fluence) is a multiplication of the outflow flux and the surface area.  
 272 Equation 2 gives the fluence emerged from the surface of bin  $jk$ .

$$273 \quad fluence_{jk} = \left( \frac{\sum_{i=0}^{n_{jk}-1} flux_i}{n_{jk}} \right)_{jk} \times A_{jk} \quad \text{Equation 2}$$

274 Which  $\left( \frac{\sum_{i=0}^{n_{jk}-1} flux_i}{n_{jk}} \right)_{jk}$  is the averaged outflow flux, and  $A_{jk}$  is the area of bin  $jk$ . At a  
 275 mapped altitude of 300 km, we calculated  $A_{jk}$  from Equation 3.

$$276 \quad A_{jk} = -(\cos \theta_2 - \cos \theta_1)_j \times (\varphi_2 - \varphi_1)_k \times r^2 \quad \text{Equation 3}$$

277 The radius  $r$  is the sum of mapped altitude and the Earth radius, in centimeters,  $r =$   
 278  $(R_E + 300) \times 10^5 \quad (cm)$ .

279 We quantitatively illustrated the variation of ionospheric O<sup>+</sup> fluence during the CME and  
 280 SIR storm phases separately by summing the fluences of all MLT-ILAT bins; For example,

$$281 \quad fluence_{(dayside)} = \sum_{j=0, k=9}^{40, 15} fluence_{jk}$$

282 The line plots in Figure 6 show the variation of measured fluence for CME moderate  
 283 storms with the solid red line, CME intense storms with the dashed red line, and SIR moderate  
 284 storms with the solid blue line. Due to the low statistics of SIR intense storms, we do not include  
 285 the fluence of SIR intense storms. The panels, from top to bottom give the total fluence covering

286 all MLT sectors, the (dusk + night) fluence measured from summing fluences of dusk and night  
287 side sectors, and the (dawn + day) fluence containing the fluences summed from dawnside and  
288 dayside bins. We have combined these sectors because we note that the dayside outflow tends to  
289 extend towards the dawn, while the nightside outflow extends towards the dusk. The error bars  
290 indicate the Standard Error of Mean (SEM).

291 We observe that the  $O^+$  fluence before the storms are roughly the same for both CME and  
292 SIR storms. For CME storms, the fluence increases by a factor of 10 in the initial phase,  
293 increases further in the main phase, and declines in the recovery phase. For the SIR storms, the  
294 fluence is about the same in the initial phase, increases in the main phase and then decreases in  
295 the recovery phase.

296 Also, we observe that intense CME storms have more  $O^+$  fluence than moderate CME  
297 storms. For moderate storms, the  $O^+$  fluence produced during the main phase is about a factor of  
298 two higher in CME storms than in SIR storms. As stated earlier, the most significant difference  
299 between the fluence in CME moderate storms with SIR moderate storms is the  $O^+$  fluence during  
300 the initial phase. The CME storms produce  $O^+$  fluence 15 times higher than SIR storms in the  
301 initial phase. This significant difference is observed in both the “day + dawn” and “dusk + night”  
302 sectors.

#### 303 4.2 $H^+$ Outflow flux

304 Figure 7 presents the averaged  $H^+$  outflow flux during CME storms. Before the storm, the  
305  $H^+$  outflow was observed on both the dayside and nightside. As with the  $O^+$ , the  $H^+$  outflow  
306 increased during the initial phase and extended in MLT and ILAT. The increased  $H^+$  outflow  
307 reaches its maximum in the main phase, and it covers all MLT sectors with ILAT between  $60^\circ$  to  
308  $80^\circ$ , even extending below  $60^\circ$  in a few bins. The flux declined in the recovery phase but still  
309 covers a wide MLT range. As with  $O^+$ , the  $H^+$  flux is stronger and reaches a lower latitude in  
310 intense storms than in moderate storms. In large storms, the extended outflow down to 50  
311 degrees in 18MLT and 6 MLT results from the auroral region.

312 Figure 8 shows the averaged  $H^+$  outflow flux for SIR storms. The spatial distribution for  
313 the  $H^+$  outflow for SIR storms is very similar to the  $O^+$  outflow. As with  $O^+$ , there is essentially  
314 no increase during the initial phase. During the main phase, the strongest outflow is in the

315 dayside, while for  $O^+$ , it was on the dawnside, but it is still strong in both regions. As for  $O^+$ , the  
316  $H^+$  outflow is stronger and reaches a lower latitude during CME than during SIR storms.

317 The line plots in Figure 9 present the variation of total  $H^+$  fluence as a function of storm  
318 phases during CME moderate (solid red line), CME intense (dashed red line), and SIR moderate  
319 (solid blue line) storms. The total fluence is almost the same in the prestorm phase. During the  
320 initial phase, the CME storms show a significant increase, while there is almost no increase for  
321 SIR moderate storms. In the main phase, the  $H^+$  fluence produced by CME and SIR storms is  
322 about the same. In the Recovery phase, the moderate SIR storms had more  $H^+$  fluence than CME  
323 moderate storms, and the fluxes are the same within the statistical error.

324 In the Recovery phase, the moderate SIR storms had more  $H^+$  fluence than CME  
325 moderate storms; however, for “dusk + night” the CME flux is inside the SIR error bar.

326 Comparing CME moderate storms with SIR moderate storms shows that the total  $H^+$   
327 fluence during the initial phase of CME storms is significantly higher than during SIR storms, in  
328 both the dayside and the nightside sectors.

## 329 **5. Solar cycle (solar EUV) and seasonal effects**

330 After studying the effect of solar wind structures on ionospheric  $O^+$  outflow, we  
331 investigate the impact of the solar cycle on storm time ionospheric  $O^+$  outflow. We divided the  
332 moderate CME storms into two groups: solar maximum and solar minimum storms. The  
333 statistics of participating storms in this study are given in Table 1. First, we prepared the MLT-  
334 ILAT plots similar to Figure 4 and calculated the total fluence. Figures 10(a) and (b) depict the  
335  $O^+$  and  $H^+$  fluences observed during moderate CME storms. The solid lines correspond to  
336 fluence levels recorded during solar maximum years, while the dashed lines represent fluence  
337 levels during solar minimum years. The fluences were computed separately for the (dusk +  
338 night) and (dawn + day) periods, as illustrated in the second and third panels from the top,  
339 respectively. Figures 10(c) and (d) illustrate the  $O^+$  and  $H^+$  fluences specifically observed during  
340 moderate CME storms restricted to solar minimum years. Here, the solid lines signify fluence  
341 levels recorded in the summer season, while the dashed lines indicate fluence levels in the winter  
342 season. The panel arrangement from top to bottom mirrors that of panels (a, b).

343 From Figure 10(a), it is clear that the total  $O^+$  fluence is higher during solar maximum  
344 than during solar minimum. The difference is particularly noticeable during the main phase of  
345 storms, where it is 2.6 times higher. In Figure 10(b), it can be seen that the total  $H^+$  fluence  
346 remains the same during both solar maximum and solar minimum. Furthermore, there is no  
347 difference in the (Day + Dawn) sector. However, in the (Dusk + Night) sector during solar  
348 minimum, more  $H^+$  fluence is detected.

349 In Figure 10 (c, d), we present the measured  $O^+$  and  $H^+$  fluences from summer season  
350 (solid lines) and winter season (dashed lines) for CME solar minimum storms. From Figure  
351 10(c), we find that the total  $O^+$  fluence is stronger in summer than in winter. The separate panels  
352 for the (day + dawn) and (dusk + night) sectors show that the dayside  $O^+$  fluence is stronger in  
353 the summer than in winter, while on the nightside, the  $O^+$  fluence is almost independent of the  
354 season. Figure 10(d) shows that in contrast to  $O^+$ , the total  $H^+$  fluence shows no overall change in  
355 the summer and winter seasons. However, on the nightside, the  $H^+$  fluences are stronger in the  
356 winter than in summer, while on the dayside, the  $H^+$  fluence is stronger in the summer than in  
357 winter.

## 358 **6. Discussion**

359 The observation that the outflow increases during the initial phase for CME storms, both  
360 on the dayside and the nightside, may explain the higher  $O^+$  observed during CME storms by  
361 Mouikis et al. (2019). CMEs are often preceded by a shock with enhanced dynamic pressure.  
362 Auroral effects from enhanced dynamic pressure have been observed previously. Brittnacher et  
363 al. (2000) show an example where the arrival of the pressure enhancement associated with a  
364 CME was observed in the aurora, with the intensification first observed on the dayside, with a  
365 nightside enhancement observed 15 minutes later. Boudouridis et al. (2003) found that the  
366 response of the size and strength of the auroral oval to a pressure enhancement was global, with a  
367 noon-midnight propagation of the effect observed for cases when the IMF is northward.  
368 Simulations indicate that enhanced dynamic pressure increases energy input to the aurora from  
369 precipitating electrons (Damiano et al., 2010), which would drive the enhanced outflow.  $O^+$   
370 outflow during the initial phase has time to convect from the dayside to the nightside plasma  
371 sheet before the enhanced convection, associated with the storm main phase, begins. That  
372 outflow from enhanced dynamic pressure may populate the plasmashet prior to a storm was

373 shown by (Kistler et al., 2016). They observed the flux of hot, energetic ( $\sim 5$  keV)  $O^+$  ions in the  
374 plasma sheet increase after a large pressure pulse hit the Earth's magnetosphere but before the  
375 start of the storm main phase. The hot  $O^+$  in the plasma sheet also preceded the observation of  $O^+$   
376 outflow coming directly from the nightside aurora. The inward convection of the hot  $O^+$  from the  
377 prestorm plasma sheet dominated the ring current pressure during the storm main phase.

378 It is also possible that differences in the main phase outflow fluence, between CMEs and  
379 SIRs, play a role in making the ring current during CMEs richer in  $O^+$ . The outflow fluence of  
380  $O^+$  during moderate CME storms is about a factor of two higher than the fluence during SIR  
381 storms, while the  $H^+$  fluence is about the same. This will lead to a higher  $O^+$  abundance  
382 throughout the magnetosphere.

383 The observed variations with solar cycle agree with the schematic model of Yau et al.  
384 (1985) and Yau et al. (1988) in which an upward shift of the ionospheric  $O^+$  source region from  
385 solar minimum to solar maximum causes a correlation between increasing ionospheric  $O^+$   
386 density and increasing F10.7 in quiet and active times. The  $O^+$  variation with storm phase is  
387 about the same during solar minimum and solar maximum, but the  $O^+$  fluence is higher during  
388 all phases. The  $H^+$  fluence showed no change between solar maximum and minimum phases on  
389 the dayside, but on the nightside, more  $H^+$  fluence is seen during solar minimum than the solar  
390 maximum.

391 Our study of the seasonal effect on storm-time ionospheric outflow was limited to the  
392 solar minimum phase (ascending and declining phases) of solar cycle 23. For the nightside  
393 sector,  $O^+$  fluence is independent of season. On the dayside, the CME storm time  $O^+$  fluence is  
394 stronger during the summer season than the winter season, in agreement with the Yau, Beckwith  
395 et al. (1985) result. However, on the nightside, there was no difference. For  $H^+$ , the nightside  
396 fluence is stronger during the winter season than in the summer season. For the dayside,  $H^+$   
397 fluence showed no seasonal effect. The stronger nightside fluence during winter may be a result  
398 of the enhanced energetic electron precipitation in the nightside region during winter (Newell et  
399 al., 1996) and is consistent with the observation of more ion beams in winter than in summer  
400 (Collin et al., 1998).

401 In this study, the net ionospheric  $H^+$  and  $O^+$  fluences were significantly less than  
402 observations from other studies (Collin et al., 1984; Cully et al., 2003; Peterson et al., 2001; Yau

403 et al., 1988). These studies were done with different instruments on different spacecraft at  
404 different altitudes and under various geomagnetic and solar cycle conditions. To have a better  
405 understanding of this discrepancy, Table 2. lists the instrumental and geomagnetic features of  
406 studies in addition to the reported  $H^+$  and  $O^+$  fluences.

407 In the column labeled “this study”, we report the FAST total averaged fluences for  $H^+$   
408 and  $O^+$  from the region with ILAT greater than  $50^\circ$ , the altitude range of 1500 km to 4200 km,  
409 and the energy range of 10 eV/e to 12000 eV/e, for prestorm times, as quiet time, and for  
410 moderate CME and SIR storms. Since our observation showed that ionospheric outflow is  
411 impacted by the solar cycle, the fluences during the solar maximum and the solar minimum  
412 phases are separated in Table 2. The next columns indicate the information from Table 1. of the  
413 Collin et al. (1984) study, Figure 3. in Yau et al. (1988), Table 5. in Peterson et al. (2001), and  
414 Figure 3. in Cully et al. (2003).

415 In Figure 11, the  $H^+$  and  $O^+$  outflow rates from the quiet time during solar minimum from  
416 different spacecraft are plotted as a function of altitude. From the plot, we see that the DE-1  
417 spacecraft from the highest altitude reported the highest values, and the FAST spacecraft with  
418 the lowest altitude reported the lowest values for  $H^+$  and  $O^+$  rates. Thus one possibility for the  
419 discrepancies is that the ions are continuously accelerated as they move up the field line and  
420 therefore, cold ions that are invisible at lower altitudes move above the low-energy instrument  
421 threshold at higher altitudes. However, the four instruments all have different low-energy  
422 thresholds, and therefore some results do not support this picture. The instrument on S3-3 had a  
423 lower energy threshold of 500 eV, significantly higher than the other instruments. In fact, as  
424 seen in the example in Figure 4, most of the outflow observed in this study is below 500 eV. The  
425 high values reported by (Cully et al., 2003) may therefore be due to difficulties in subtracting the  
426 upflow contribution of precipitating particles, a problem avoided in this study by using the  
427 dynamic high energy cut-off. The Akebono/SMS has the lowest energy threshold, of 1 eV, but  
428 also the lowest high-energy threshold, 70 eV. Thus, the agreement with FAST for  $O^+$  may be  
429 due to measuring the outflow with a higher contribution of low energies, and less contribution of  
430 higher energies. The large difference between the FAST measurements and Akebono for  $H^+$   
431 indicates a significant contribution below 10 eV. The better agreement between Akebono and  
432 Polar with DE-1 for  $H^+$  than for  $O^+$  may indicate that the majority of the  $H^+$  reaches detectable  
433 energies at a lower altitude than the  $O^+$ . Still, the many differences between the different data

434 sets make it impossible to completely reconcile the discrepancies in the total fluence  
435 measurements.

## 436 **7. Summary Conclusion**

437 In this paper, we performed a comprehensive analysis to determine the variation of  
438 ionospheric  $O^+$  and  $H^+$  outflow as a function of geomagnetic storm for CME and SIR storms. We  
439 used FAST and OMNI data from 1996 to 2008, covering the solar cycle 23. In this period, 139  
440 geomagnetic storms with  $Dst < -50nT$  were identified that had good FAST data coverage and  
441 were driven by clear CME or SIR solar wind structures. We excluded storms with undetermined  
442 drivers and storms with complex drivers. We found that:

443 1-  $O^+$  and  $H^+$  outflows increase in the initial phase of CME storms but do not increase until  
444 the main phase in SIR storms; For CME storms, the outflow in the initial phase has time to reach  
445 the plasma sheet prior to the main phase, and therefore may explain why CME storms have more  
446  $O^+$  than SIR storms.

447 2- in both CME and SIR storms, the maximum outflow occurs in the main phase and then  
448 declines in the recovery phase.

449 3- In dividing the storms by  $Dst$ , intense CME storms ( $Dst < -150$ ) produce more  $O^+$  and  $H^+$   
450 outflow than moderate storms ( $Dst > -150$ ).

451 4- The  $O^+$  outflows produced by moderate CME are slightly larger than SIR storms during  
452 main phase and comparable in the recovery phases. The  $H^+$  is comparable during all phases.

453 5-  $O^+$  outflow increases with increasing solar EUV flux, while  $H^+$  outflow in the dayside is  
454 independent of solar EUV flux while in the nightside decreases with increasing solar EUV.

455 6- Dayside  $O^+$  and  $H^+$  outflows increase in summer season. The nightside  $O^+$  outflow is  
456 independent of the season, while the nightside  $H^+$  outflow increases in winter.

457 7- The differences between the FAST  $O^+$  and  $H^+$  total fluence with measurements from DE-  
458 1 by Yau et al. (1988) suggest that the FAST measurements, with a low energy cutoff of 10 eV,  
459 do not represent the total outflow flux. It is likely that  $O^+$  and  $H^+$  continue to be energized at  
460 altitudes above the FAST spacecraft.

## 461 **Acknowledgements**

462 The work at the University of New Hampshire was supported by the National  
463 Aeronautics and Space Administration under grants 80NSSC19K0073, 80NSSC20K0594,  
464 NNX15AQ91G, NSF 1502937, 80NSSC19K0363. The FAST(TEAMS) data are available  
465 via <https://spdf.gsfc.nasa.gov/pub/data/fast/teams/12/pa/>

466

## 467 **References**

468 Borovsky, J. E., & Denton, M. H. (2006). Differences between CME-driven storms and CIR-  
469 driven storms. *Journal of Geophysical Research: Space Physics*, *111*(7).  
470 <https://doi.org/10.1029/2005JA011447>

471 Boudouridis, A., Zesta, E., Lyons, L. R., Anderson, P. C., Lummerzheim, D., & Boudouridis,  
472 C. : (2003). Effect of solar wind pressure pulses on the size and strength of the auroral oval.  
473 *Journal of Geophysical Research*, *108*(A4), 8012. <https://doi.org/10.1029/2002JA009373>

474 Brittnacher, M., Wilber, M., Fillingim, M., Chua, D., Parks, G., Spann, J., & Germany, G.  
475 (2000). Global auroral response to a solar wind pressure pulse. *Advances in Space*  
476 *Research*, *25*(7–8), 1377–1385. [https://doi.org/10.1016/S0273-1177\(99\)00647-X](https://doi.org/10.1016/S0273-1177(99)00647-X)

477 Carlson, C W, Mcfadden, J. P., Turin, P., Curtis, D. W., & Martin, L. (2001). The electron and  
478 ion plasma experiment for FAST. *Space Science Reviews*, *98*, 33–66.

479 Carlson, Charles W. (1998). The Fast Auroral Snapshot Explorer. *Geophysical Research Letters*,  
480 *25*(12), 2013–2016. <https://doi.org/10.1029/91EO00202>

481 Collin, H. L., Sharp, R. D., & Shelley, E. G. (1984). The magnitude and composition of the  
482 outflow of energetic ions from the ionosphere. *Journal of Geophysical Research*, *89*(A4),  
483 2185–2194. <https://doi.org/10.1029/JA089iA04p02185>

484 Collin, H. L., Peterson, W. K., Lennartsson, O. W., & Drake, J. F. (1998). The seasonal variation  
485 of auroral ion beams. *Geophysical Research Letters*, *25*(21), 4071–4074.  
486 <https://doi.org/10.1029/1998GL900090>

487 Cully, C. M., Donovan, E. F., Yau, A. W., & Arkos, G. G. (2003). Akebono/suprathermal mass  
488 spectrometer observations of low-energy ion outflow: Dependence on magnetic activity and  
489 solar wind conditions. *Journal of Geophysical Research: Space Physics*, *108*(A2).  
490 <https://doi.org/10.1029/2001JA009200>

491 Damiano, P. A., Brambles, O. J., Lotko, W., Zhang, B., Wiltberger, M., & Lyon, J. (2010).

492 Effects of solar wind dynamic pressure on the ionospheric O<sup>+</sup> fluence during the 31 August

493 2005 storm. *Journal of Geophysical Research*, 115, 0–07.  
494 <https://doi.org/10.1029/2010JA015583>

495 Elphic, R. C., Means, J. D., Snare, R. C., Strangeway, R. J., Kepko, L., & Ergun, R. E. (2001).  
496 Magnetic field instruments for the Fast Auroral Snapshot Explorer. *Space Science Reviews*,  
497 98, 151–168.

498 Ergun, R. E., Carlson, C. W., Mozer, F. S., Delory, G. T., Temerin, M., Mcfadden, J. P., et al.  
499 (2001). The FAST satellite fields instruments. *Space Science Reviews*, 98, 67–91.

500 Greenspan, M. E., & Hamilton, D. C. (2002). Relative contributions of H<sup>+</sup>  
501 and O<sup>+</sup> to the ring current energy near magnetic storm maximum.  
502 <https://doi.org/10.1029/2001JA000155>

503 Hamilton, D. C., Gloeckler, G., Ipavich, F. M., Stüdemann, W., Wilken, B., & Kremser, G.  
504 (1988). Ring current development during the great geomagnetic storm of February 1986.  
505 *Journal of Geophysical Research*, 93(A12), 14343.  
506 <https://doi.org/10.1029/ja093ia12p14343>

507 Hatch, S. M., Moretto, T., Lynch, K. A., Laundal, K. M., Gjerloev, J. W., & Lund, E. J. (2020).  
508 The relationship between cusp region ion outflows and east-west magnetic field fluctuations  
509 at 4000-km altitude. *Journal of Geophysical Research: Space Physics*, 125(3).  
510 <https://doi.org/10.1029/2019JA027454>

511 Jian, L., Russell, C. T., Luhmann, J. G., & Skoug, R. M. (2006a). Properties of interplanetary  
512 coronal mass ejections at one AU during 1995 - 2004. *Solar Physics*, 239(1–2), 393–436.  
513 <https://doi.org/10.1007/s11207-006-0133-2>

514 Jian, L., Russell, C. T., Luhmann, J. G., & Skoug, R. M. (2006b). Properties of stream  
515 interactions at one AU during 1995 - 2004. *Solar Physics*, 239(1–2), 337–392.  
516 <https://doi.org/10.1007/s11207-006-0132-3>

517 Kistler, L. M., Mouikis, C. G., Klecker, B., & Dandouras, I. (2010). Cusp as a source for oxygen  
518 in the plasma sheet during geomagnetic storms. *Journal of Geophysical Research: Space*  
519 *Physics*, 115(3). <https://doi.org/10.1029/2009JA014838>

520 Kistler, L. M., Mouikis, C. G., & Genestreti, K. J. (2013). In-flight calibration of the  
521 Cluster/CODIF sensor. *Geoscientific Instrumentation, Methods and Data Systems*, 2(2),  
522 225–235. <https://doi.org/10.5194/gi-2-225-2013>

523 Kistler, L. M., Mouikis, C. G., Spence, H. E., Menz, A. M., Skoug, R. M., Funsten, H. O., et al.  
524 (2016). The source of O<sup>+</sup> in the storm time ring current. *Journal of Geophysical Research:*  
525 *Space Physics*, 121(6), 5333–5349. <https://doi.org/10.1002/2015JA022204>

526 Kistler, L. M., Mouikis, C. G., Asamura, K., Yokota, S., Kasahara, S., Miyoshi, Y., et al. (2019).  
527 Cusp and nightside auroral sources of O<sup>+</sup> in the plasma sheet. *Journal of Geophysical*  
528 *Research: Space Physics*, 124(12), 10036–10047. <https://doi.org/10.1029/2019JA027061>

529 Klumpar, D. M., Möbius, E., Kistler, L. M., Popecki, M., Hertzberg, E., Crocker, K., et al.  
530 (2001). The Time-of-flight Energy, Angle, Mass Spectrograph (TEAMS) experiment for  
531 FAST. *Space Science Reviews*, 98(1–2), 197–219.  
532 <https://doi.org/10.1023/A:1013127607414>

533 Liao, J., Kistler, L. M., Mouikis, C. G., Klecker, B., Dandouras, I., & Zhang, J. C. (2010).  
534 Statistical study of O<sup>+</sup> transport from the cusp to the lobes with Cluster CODIF data.  
535 *Journal of Geophysical Research: Space Physics*, 115(12).  
536 <https://doi.org/10.1029/2010JA015613>

537 Maggiolo, R., & Kistler, L. M. (2014). Spatial variation in the plasma sheet composition:  
538 Dependence on geomagnetic and solar activity. *Journal of Geophysical Research: Space*  
539 *Physics*, 119(4), 2836–2857. <https://doi.org/10.1002/2013JA019517>

540 Matamba, T. M., & Habarulema, J. B. (2018). Ionospheric responses to CME- and CIR-driven  
541 geomagnetic storms along 30°E–40°E over the African sector from 2001 to 2015. *Space*  
542 *Weather*, 16(5), 538–556. <https://doi.org/10.1029/2017SW001754>

543 Mouikis, C. G., Kistler, L. M., Liu, Y. H., Klecker, B., Korth, A., & Dandouras, I. (2010). H<sup>+</sup>  
544 and O<sup>+</sup> content of the plasma sheet at 15–19 Re as a function of geomagnetic and solar  
545 activity. *Journal of Geophysical Research: Space Physics*, 115(12).  
546 <https://doi.org/10.1029/2010JA015978>

547 Mouikis, C. G., Bingham, S. T., Kistler, L. M., Farrugia, C. J., Spence, H. E., Reeves, G. D., et  
548 al. (2019). The storm-time ring current response to ICMEs and CIRs Using Van Allen  
549 Probe observations. *Journal of Geophysical Research: Space Physics*, 124(11), 9017–9039.  
550 <https://doi.org/10.1029/2019JA026695>

551 Newell, P. T., Feldstein, Y. L., Galperin, Y. I., & Meng, C.-I. (1996). Correction to “Morphology  
552 of nightside precipitation” by Patrick T. Newell, Yasha I. Feldstein, Yuri I. Galperin, and

553 Ching-I. Meng. *Journal of Geophysical Research: Space Physics*, 101(A8), 17419–17421.  
554 <https://doi.org/10.1029/96ja02055>

555 Peterson, W. K., Coilin, H. L., Yau, A. W., & Lennartsson, O. W. (2001). Polar/Toroidal  
556 imaging mass-angle spectrograph observations of suprathermal ion outflow during solar  
557 minimum conditions. *Journal of Geophysical Research: Space Physics*, 106(4), 6059–6066.  
558 <https://doi.org/10.1029/2000ja003006>

559 Peterson, W. K., Collin, H. L., Lennartsson, O. W., & Yau, A. W. (2006). Quiet time solar  
560 illumination effects on the fluxes and characteristic energies of ionospheric outflow.  
561 *Journal of Geophysical Research: Space Physics*, 111(11).  
562 <https://doi.org/10.1029/2005JA011596>

563 Richardson, I. G., & Cane, H. v. (2010). Near-earth interplanetary coronal mass ejections during  
564 solar cycle 23 (1996 - 2009): Catalog and summary of properties. *Solar Physics*, 264(1),  
565 189–237. <https://doi.org/10.1007/s11207-010-9568-6>

566 Sharp, R. D., Johnson, R. G., Shelley, E. G., & Harris, K. K. (1974). Energetic O<sup>+</sup> ions in the  
567 magnetosphere. *Journal of Geophysical Research*, 79(13), 1844–1850.  
568 <https://doi.org/10.1029/ja079i013p01844>

569 Sharp, R. D., Johnson, R. G., & Shelley, E. G. (1974). Satellite measurements of auroral alpha  
570 particles. *Journal of Geophysical Research*, 79(34), 5167–5170.  
571 <https://doi.org/10.1029/ja079i034p05167>

572 Shelley, E. G., Johnson, R. G., & Sharp, R. D. (1972). Satellite observations of energetic heavy  
573 ions during a geomagnetic storm. *Journal of Geophysical Research*, 77(31), 6104–6110.  
574 <https://doi.org/10.1029/ja077i031p06104>

575 Tsurutani, B. T., McPherron, R. L., Gonzalez, W. D., Lu, G., Gopalswamy, N., & Guarnieri, F.  
576 L. (2006). Magnetic storms caused by corotating solar wind streams. In *Geophysical*  
577 *Monograph Series* (Vol. 167, pp. 1–17). Blackwell Publishing Ltd.  
578 <https://doi.org/10.1029/167GM03>

579 Wilson, G. R., Ober, D. M., Germany, G. A., & Lund, E. J. (2004). Nightside auroral zone and  
580 polar cap ion outflow as a function of substorm size and phase. *Journal of Geophysical*  
581 *Research: Space Physics*, 109(A2), 1–18. <https://doi.org/10.1029/2003JA009835>

582 Yau, A. W., Shelley, E. G., Peterson, W. K., & Lenchyshyn, L. (1985). Energetic auroral and  
583 polar ion outflow at DE 1 altitudes: Magnitude, composition, magnetic activity dependence,

584 and long-term variations. *Journal of Geophysical Research*, 90(A9), 8417.  
 585 <https://doi.org/10.1029/ja090ia09p08417>

586 Yau, A. W., Beckwith, P. H., Peterson, W. K., & Shelley, E. G. (1985). Long-term (solar cycle)  
 587 and seasonal variations of upflowing ionospheric ion events at DE1 altitudes. *Journal of*  
 588 *Geophysical Research*, 90(A7), 6395. <https://doi.org/10.1029/ja090ia07p06395>

589 Yau, A. W., Peterson, W. K., & Shelley, E. G. (1988). Quantitative parametrization of energetic  
 590 ionospheric ion outflow. *American Geophysical Union*, 211–217.  
 591 <https://doi.org/10.1029/gm044p0211>

592 Young, D. T., Balsiger, H., & Geiss, J. (1982). Correlations of magnetospheric ion composition  
 593 with geomagnetic and solar activity. *Journal of Geophysical Research*, 87(A11), 9077.  
 594 <https://doi.org/10.1029/ja087ia11p09077>

595 Zhao, K., Kistler, L. M., Lund, E. J., Nowrouzi N., Kitamura, N., & Strangeway, R. J. (2020).  
 596 Factors controlling O<sup>+</sup> and H<sup>+</sup> outflow in the cusp during a geomagnetic storm:  
 597 FAST/TEAMS observations. *Geophysical Research Letter*, 47(11).  
 598 <https://doi.org/10.1029/2004JA010829>

600 **Tables**

601 *Table 1. Geomagnetic storms with identified drivers from 1996 to 2008.*

	TOTAL	CME	SIR
<b>total storms</b>	139	104	35
<b>intense storm(I-storms)</b>	27	26	1
<b>moderate storm(M-storms)</b>	112	78	34
<b>M-storm in maximum phase</b>	45	37	8
		Summer: 15	Summer: 4
		Winter: 21	Winter: 3
		Summer and winter: 1	Summer and winter: 1
<b>M- storm in minimum phase</b>	67	41	26
		Summer: 15	Summer: 11
		Winter: 20	Winter: 14
		Summer and winter: 6	Summer and winter: 1

			This Study <sup>1</sup>	Collin <sup>2</sup>	Yau <sup>3</sup>	Peterson <sup>4</sup>	Cully <sup>5</sup>
<b>Spacecraft</b>			FAST (TEAMS)	S3-3 (Lockheed)	DE-1 (EICS)	Polar (TIMAS)	Akebono (SMS)
<b>Data years</b>			1996-08 to 2009-12	1983-02 to 1984-05	1981-09 to 1984-05	1996-04 to 1998-09	1989-10 to 1998-09
<b>Quiet time</b>			$K_p \leq 3$ and 24 hours before initiating of storms	$K_p \leq 3$ 4-dayas after $Dst > -30nT$	$K_p \leq 2$	$0 \leq Kp \leq 7$ With $\overline{K_p} = 2 -$	$K_p \leq 2$
<b>Active time</b>			three phases of CME and SIR moderate storms	$3 < K_p \leq 5$	$K_p \geq 3$		$K_p \geq 3$
<b>Altitude(km)</b>			1500-4200	5000-8000	16000- 23000	6000-8000	6000-10000
<b>Energy(eV/e)</b>			10-12000	500-16000	10-17000	15-33000	1-70
<b>ILAT</b>			$> 50^\circ$	$> 60^\circ$	$> 56^\circ$	$> 55^\circ$	$> 65^\circ$
<b>Data from Hemisphere(s)</b>			North, South	North, South	North, South	South	North
<b>H<sup>+</sup> rate (s<sup>-1</sup>)</b>	<b>Solar maximum</b>	<b>Active</b>	$2.29 \times 10^{24}$		$8.5 \times 10^{25}$		$7 \times 10^{25}$
		<b>Quiet</b>	$2.63 \times 10^{23}$		$2.9 \times 10^{25}$		$3.1 \times 10^{25}$
	<b>Solar minimum</b>	<b>Active</b>	$2.15 \times 10^{24}$	$3.0 \times 10^{25}$	$8.5 \times 10^{25}$		$2.6 \times 10^{25}$
		<b>Quiet</b>	$2.26 \times 10^{23}$	$1.1 \times 10^{25}$	$1.7 \times 10^{25}$	$2.4 \times 10^{24}$	$1.5 \times 10^{25}$
<b>O<sup>+</sup> rate (s<sup>-1</sup>)</b>	<b>Solar maximum</b>	<b>Active</b>	$4.62 \times 10^{24}$		$2.4 \times 10^{26}$		$7.5 \times 10^{25}$
		<b>Quiet</b>	$5.97 \times 10^{23}$		$2.1 \times 10^{25}$		$1.2 \times 10^{25}$
	<b>Solar minimum</b>	<b>Active</b>	$2.15 \times 10^{24}$	$4.2 \times 10^{25}$	$8.85$ $\times 10^{25}$		$4 \times 10^{24}$
		<b>Quiet</b>	$1.89 \times 10^{23}$	$0.27 \times 10^{25}$	$4.8 \times 10^{25}$	$3 \times 10^{24}$	$2.9 \times 10^{23}$

<sup>1</sup> From observations reported in this paper.

<sup>2</sup> From Table 1. in (Collin et al., 1984).

<sup>3</sup> From Figure 3. in (Yau et al., 1988).

<sup>4</sup> From Table 5. in (Peterson et al., 2001).

<sup>5</sup> From Figure 3. in (Cully et al., 2003)

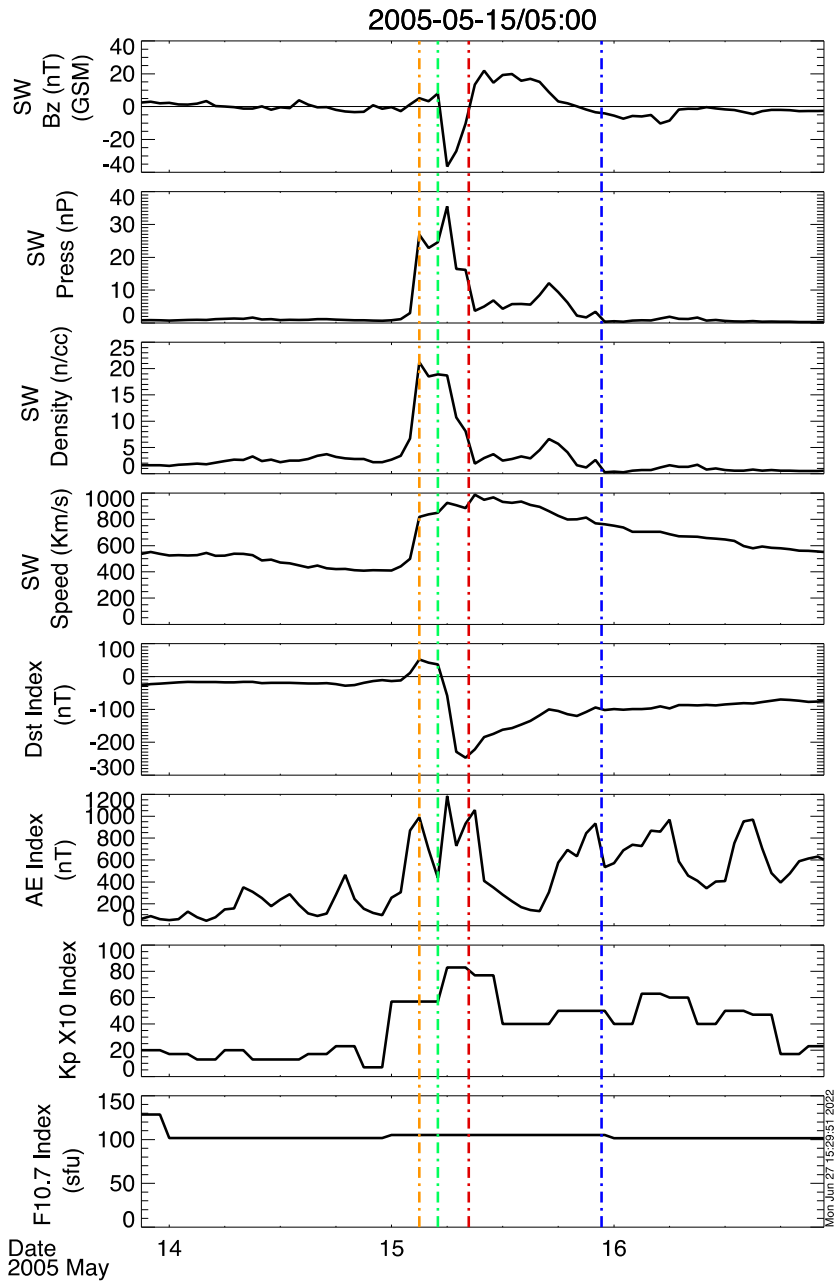


Figure 1. The solar wind parameters during a classical storm. The vertical lines present the storm critical times; the orange line denotes the increase time, the green line shows the onset time, the red line gives the time of minimum Dst\*, and the blue line recovery time.

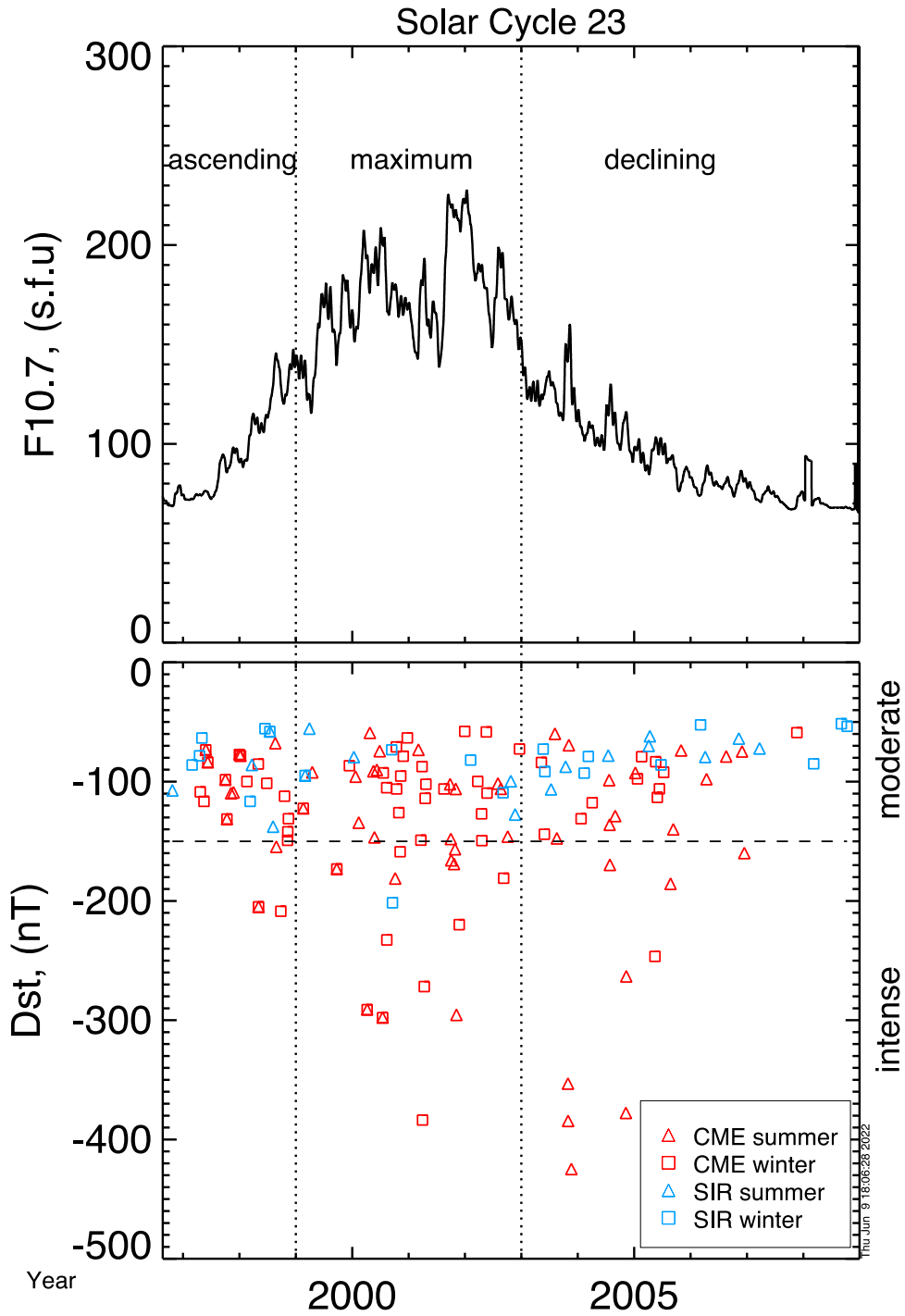


Figure 2. The top panel shows the F10.7 index for solar cycle 23. The vertical lines separate the solar cycle phases. The bottom panel shows the minimum Dst for storms, ICME (red) and SIR (blue). The horizontal dashed line separates the moderate storms from intense storms.

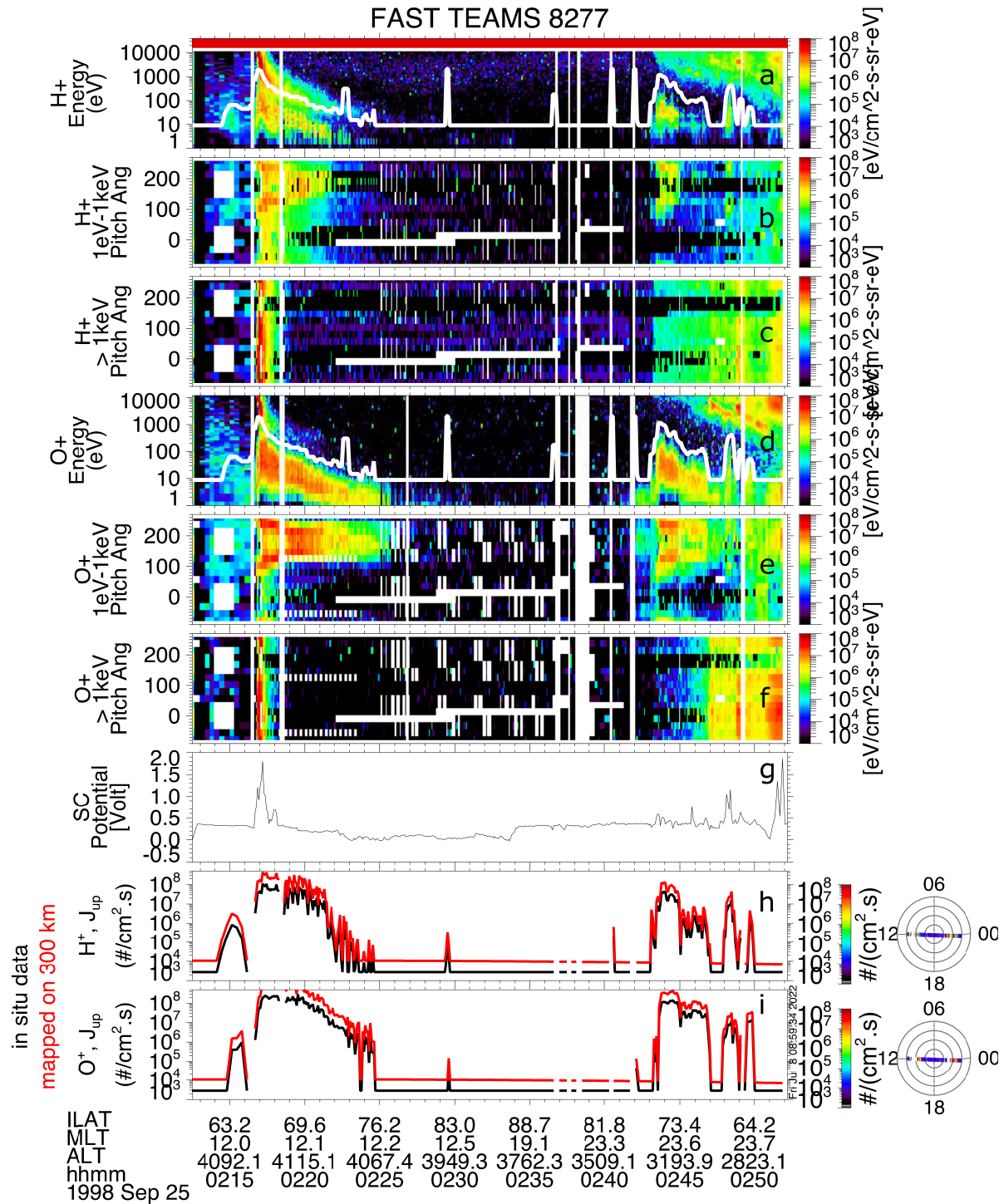


Figure 3. TEAMS summary plot for  $O^+$  and  $H^+$  data from orbit 8277. Panels (a, b, c, h) show the energy spectrogram, pitch angle spectrogram for low energy, pitch angle spectrogram for high energy and in situ outflow flux (black), and mapped outflow flux (red) for  $H^+$  ions. Similar plots for  $O^+$  ions are presented in panels (d, e, f, i). The spacecraft potential is plotted in panel (g). The white lines in panels (a) and (d) represent the upper energy cutoff.

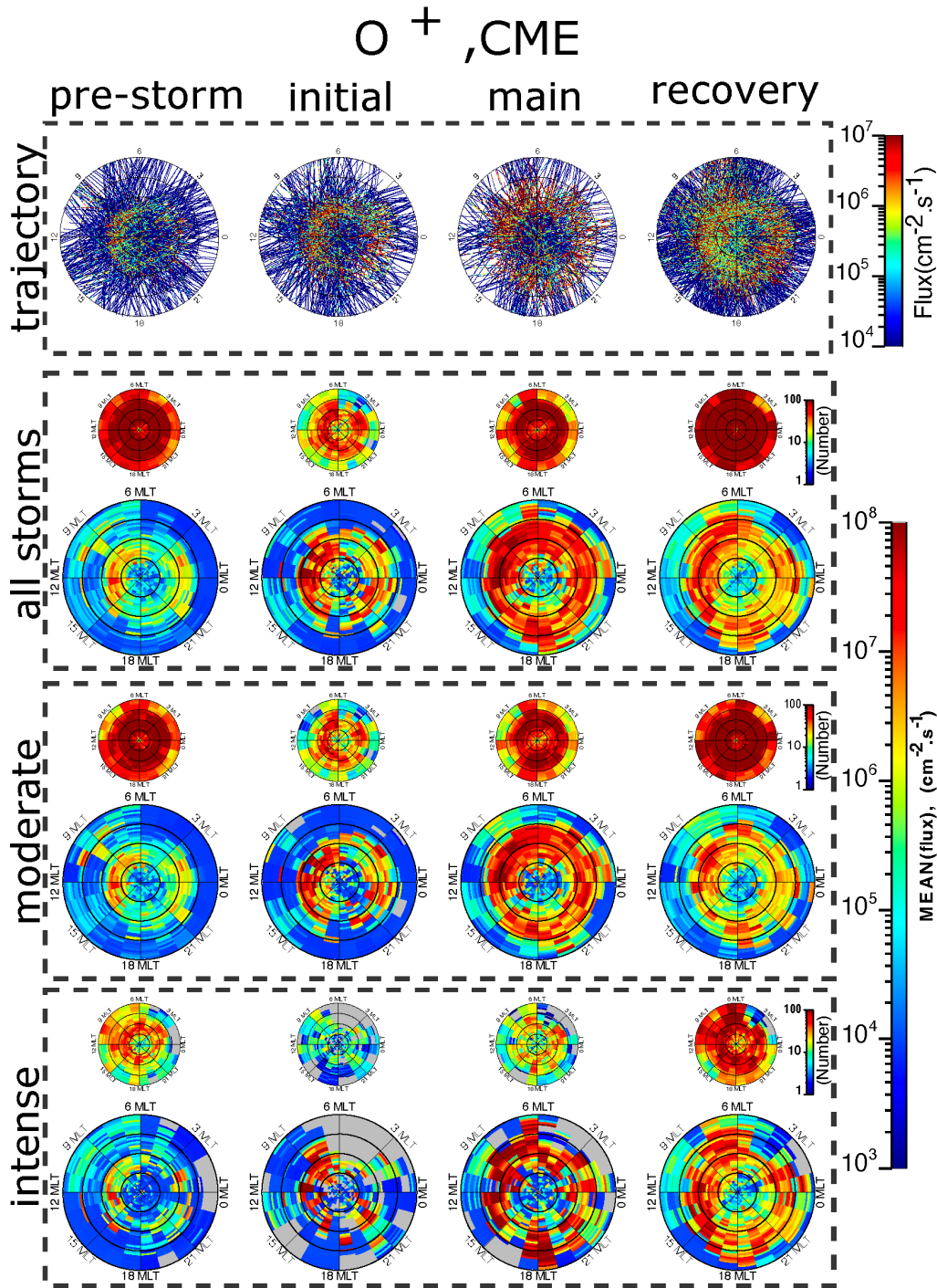


Figure 4. The first row from the top shows the  $O^+$  outflow flux during CME-driven storms along the FAST trajectory before the storm and then for three storm phases. In the second to the fourth row, the big globe plots contain the averaged outflow flux in each MLT-ILAT bin for all classical storms in the second row, for moderate storms with  $-150 \text{ nT} \leq Dst_{\text{minimum}} < -50 \text{ nT}$  in the third row, and intense storms without  $Dst_{\text{minimum}} \leq -150 \text{ nT}$  in the bottom row. The small globe plots on the top of big plots present the number of data points in each MLT-ILAT bin. The long color bar on the right shows the averaged outflow flux in the bins of big globe plots and three short color bars show the number of data points in each bin of small globe plots.

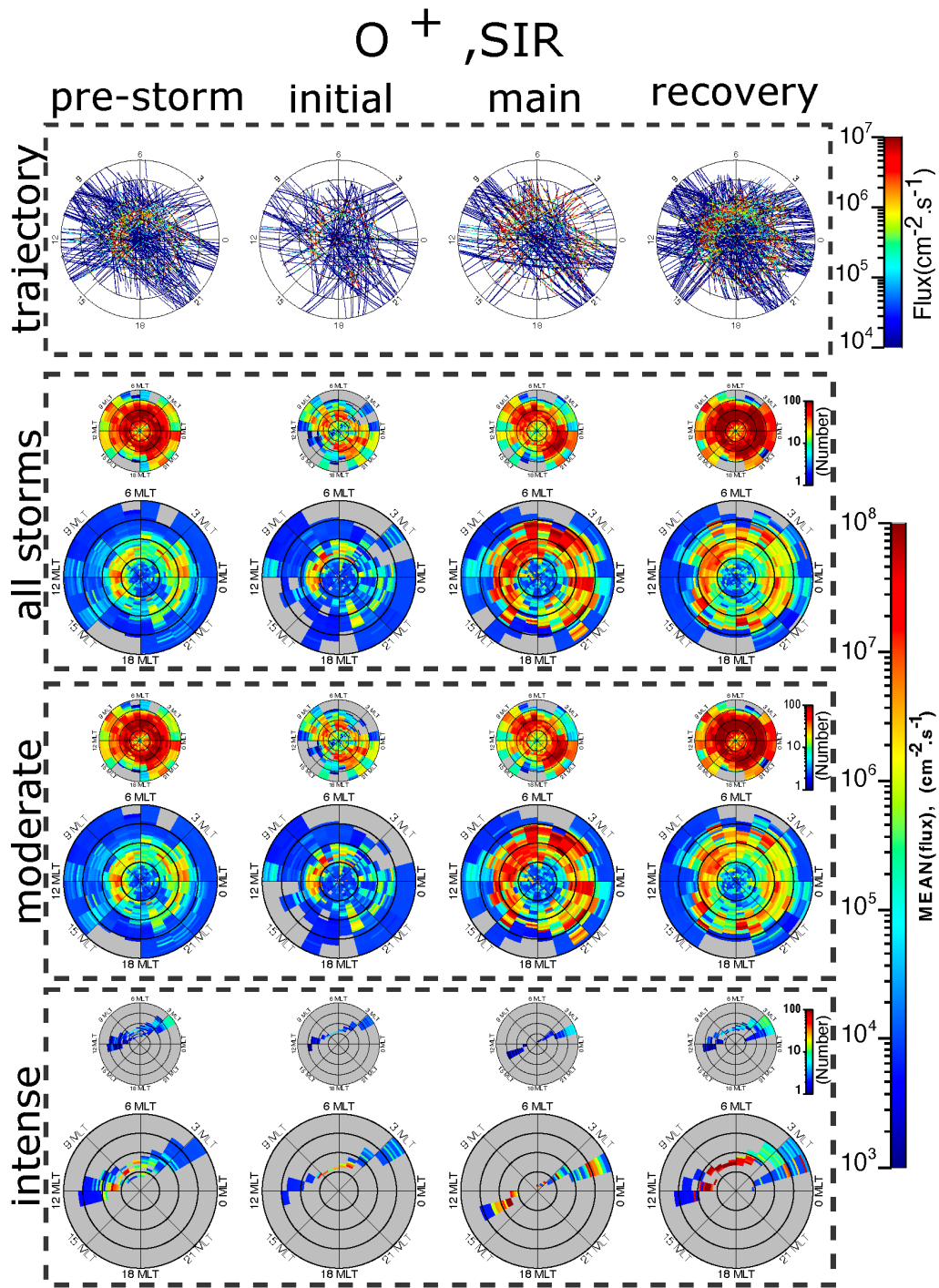


Figure 5. The  $O^+$  outflow flux for SIR-driven storms. The format is the same as for Figure 4.

610

611

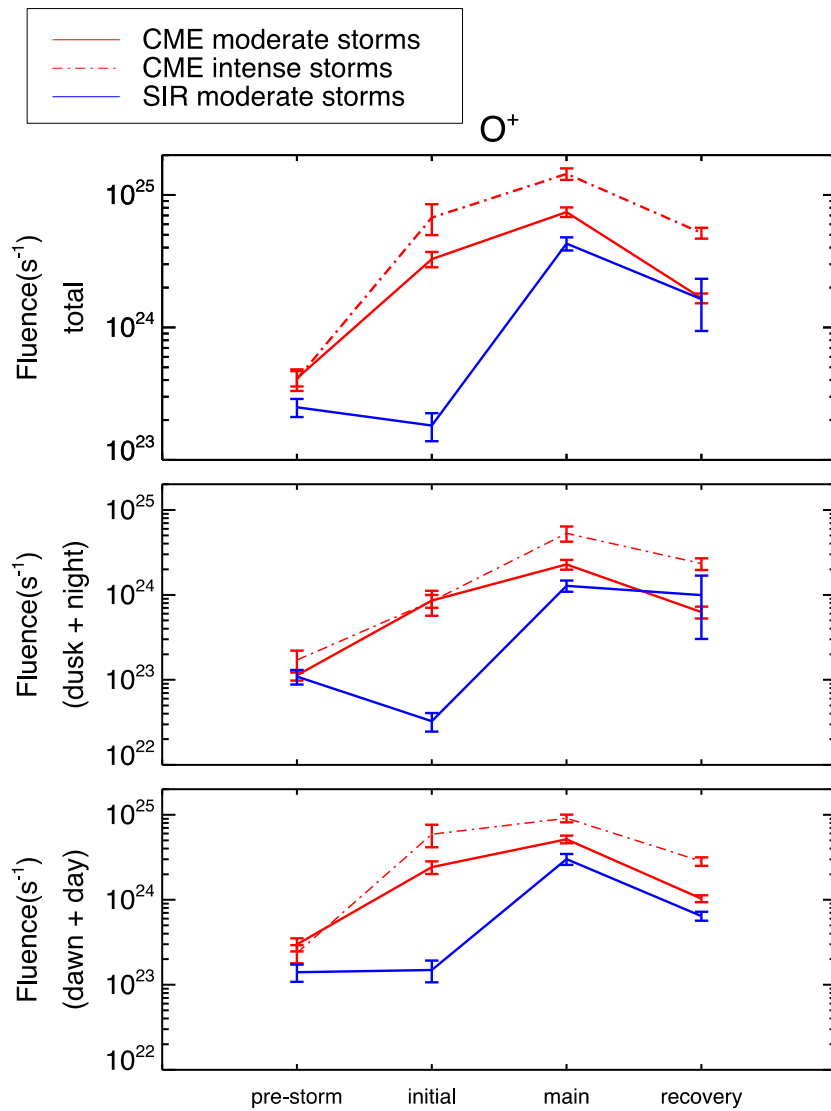


Figure 6. The total  $O^+$  fluence for CME storms in red and SIR storms in blue. The solid lines indicate the fluence during moderate storms and the dashed line during intense storms.

612

613

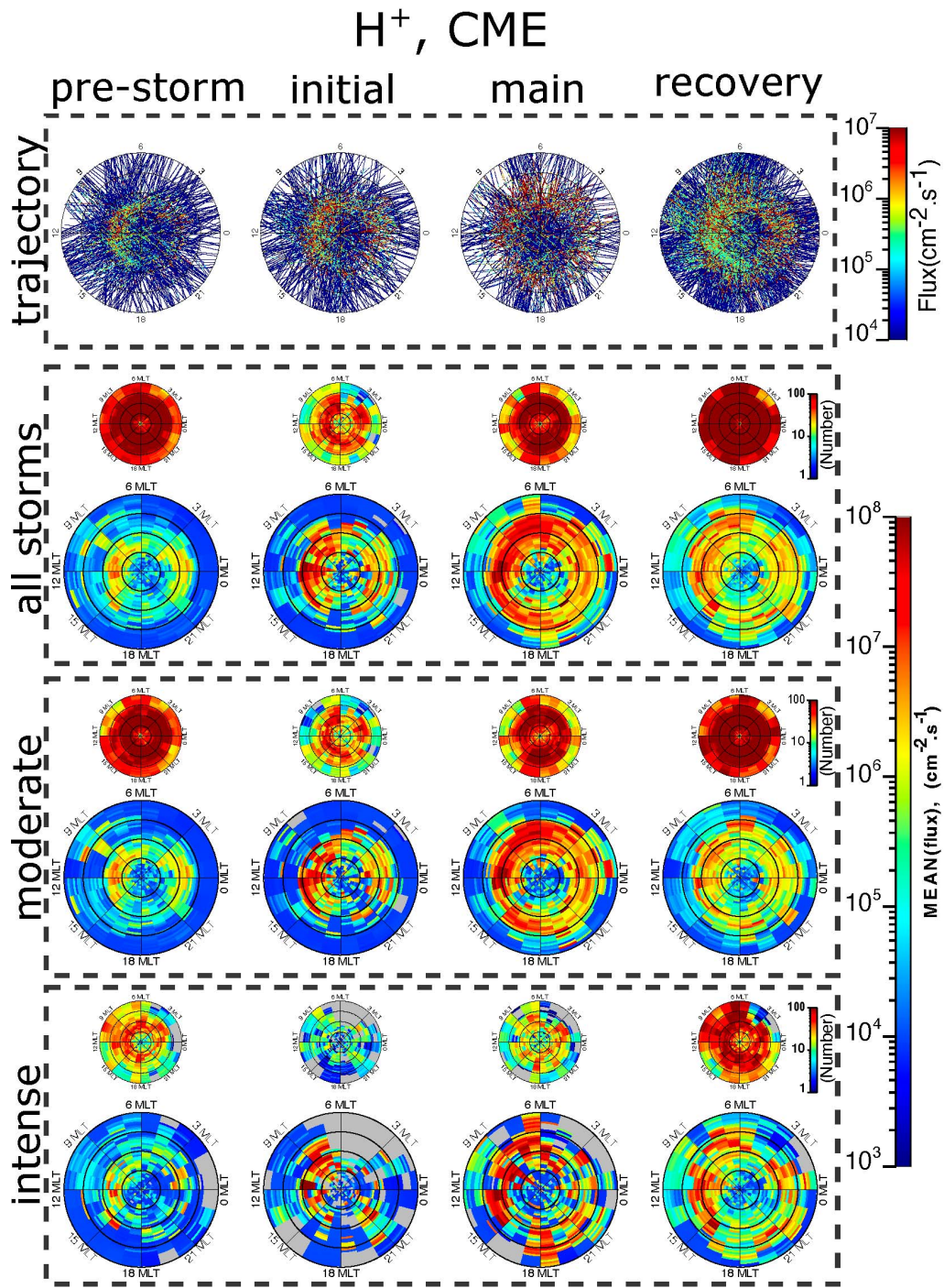


Figure 7. The H<sup>+</sup> outflow flux for CME-driven storms. The format is the same as Figure 4

614

615

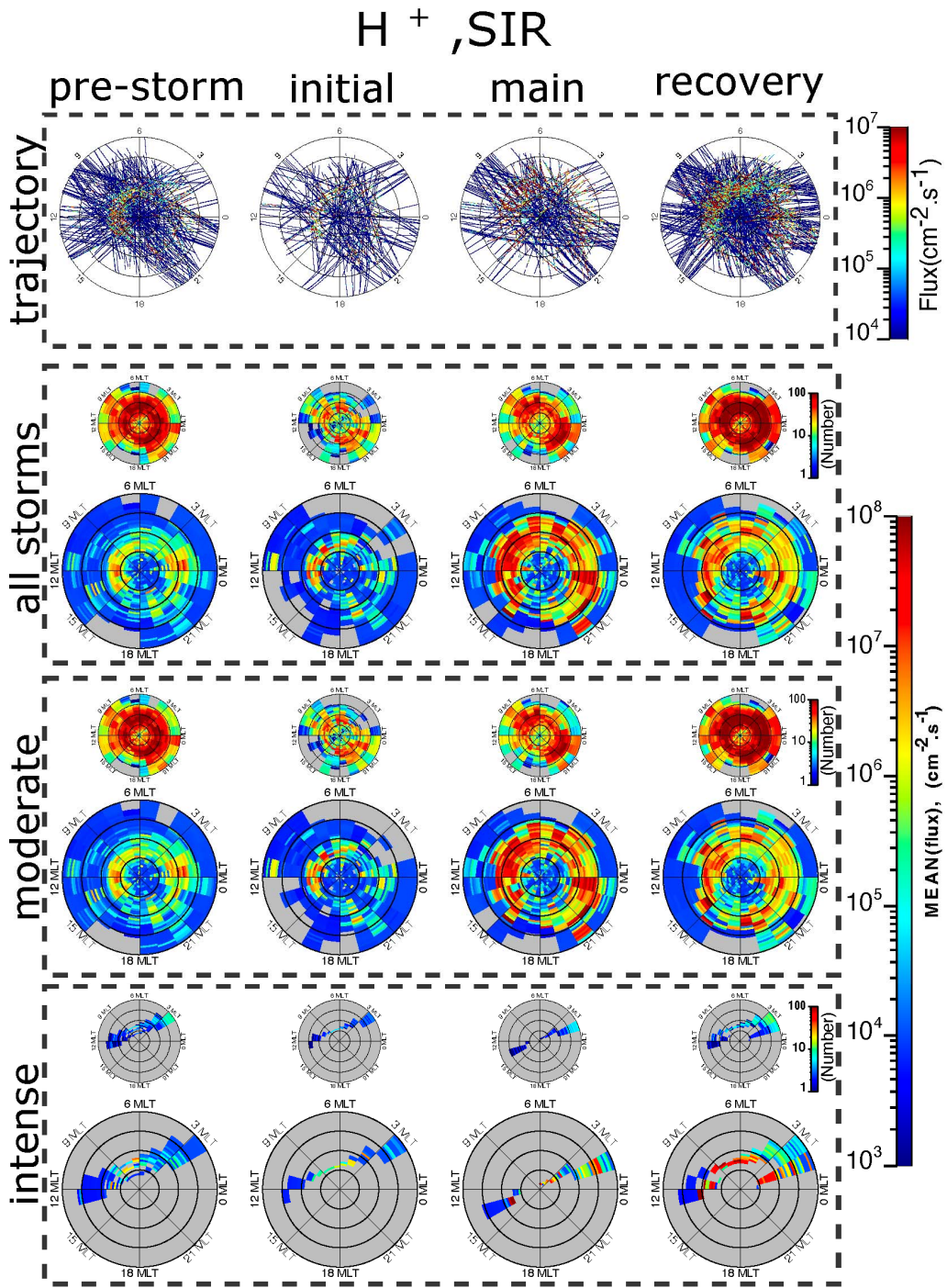


Figure 8. The  $H^+$  outflow flux for SIR-driven storms. The format is the same as in Figure 4.

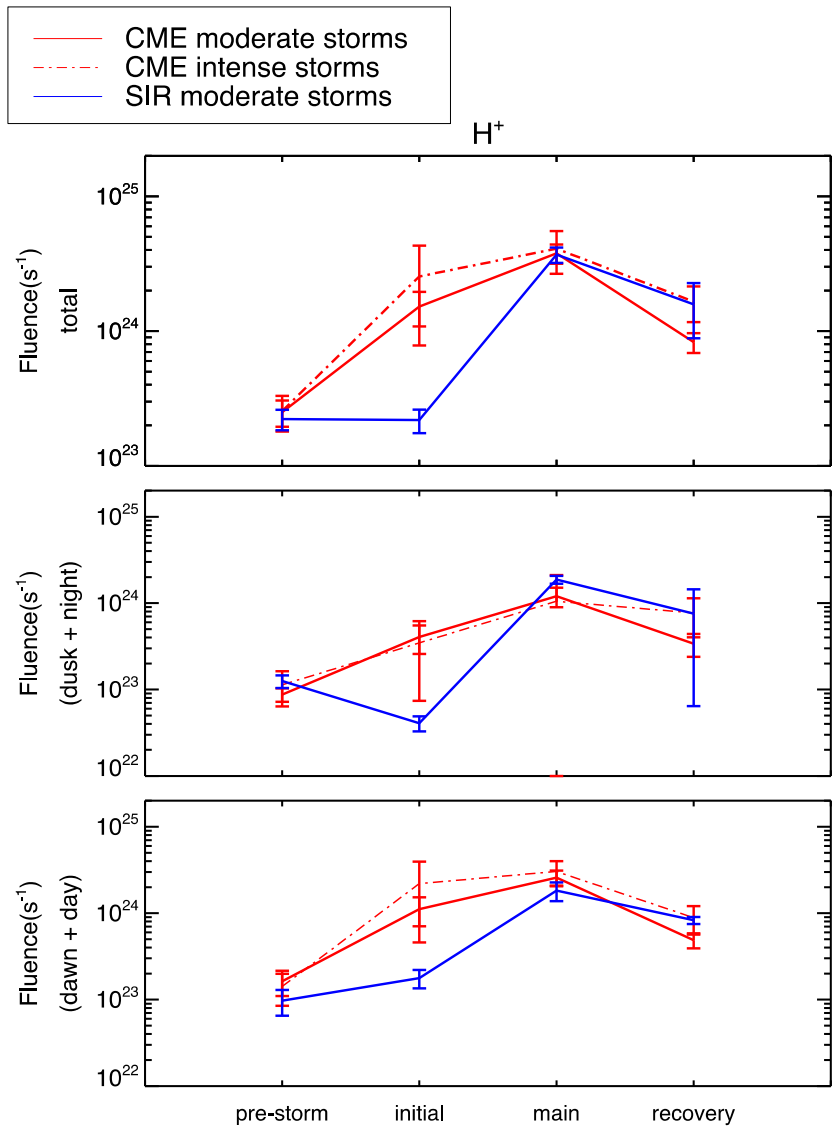


Figure 9. The total  $H^+$  fluence for CME storms in red and SIR storms in blue. The solid lines indicate the fluence during moderate storms and the dashed line during intense storms.

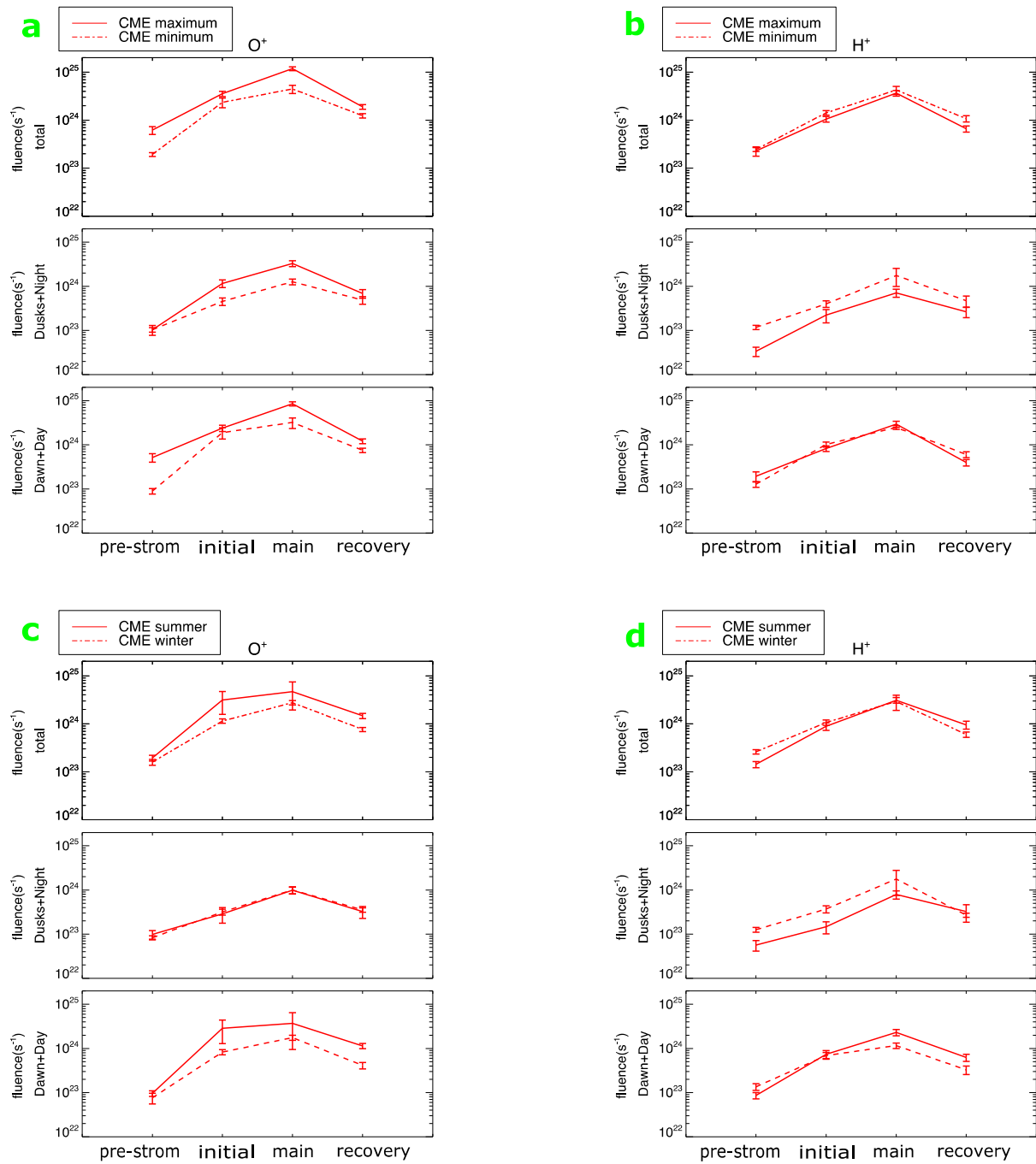


Figure 10. Panel (a, b) show the total  $O^+$  and  $H^+$  fluences for moderate CME storms. The solid lines indicate the fluence during storms of solar maximum years, and the dashed lines during storms of solar minimum. The calculated fluences, separately for (dusk + night) and (dawn + day), are shown in the second and third panels from the top. Panels (c, d) show the  $O^+$  and  $H^+$  fluences for moderate CME storms in solar minimum years. The solid lines indicate the summer season fluence, and the dashed present the winter season fluence. Panels from the top to the bottom are the same as panels (a, b).

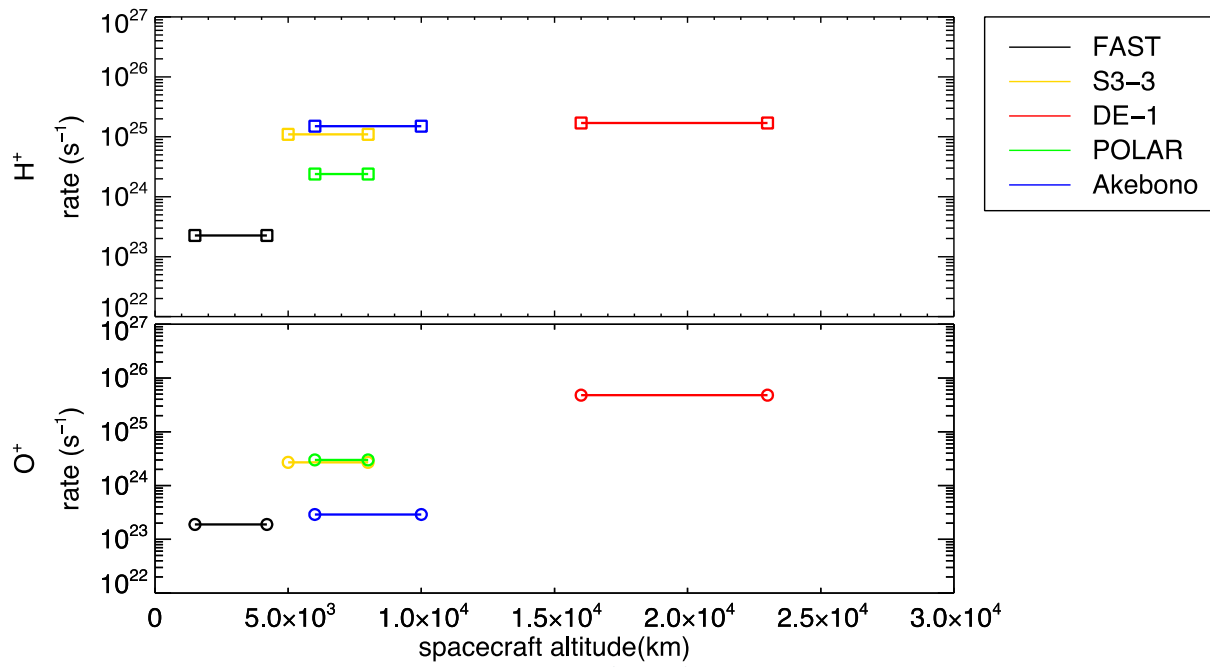
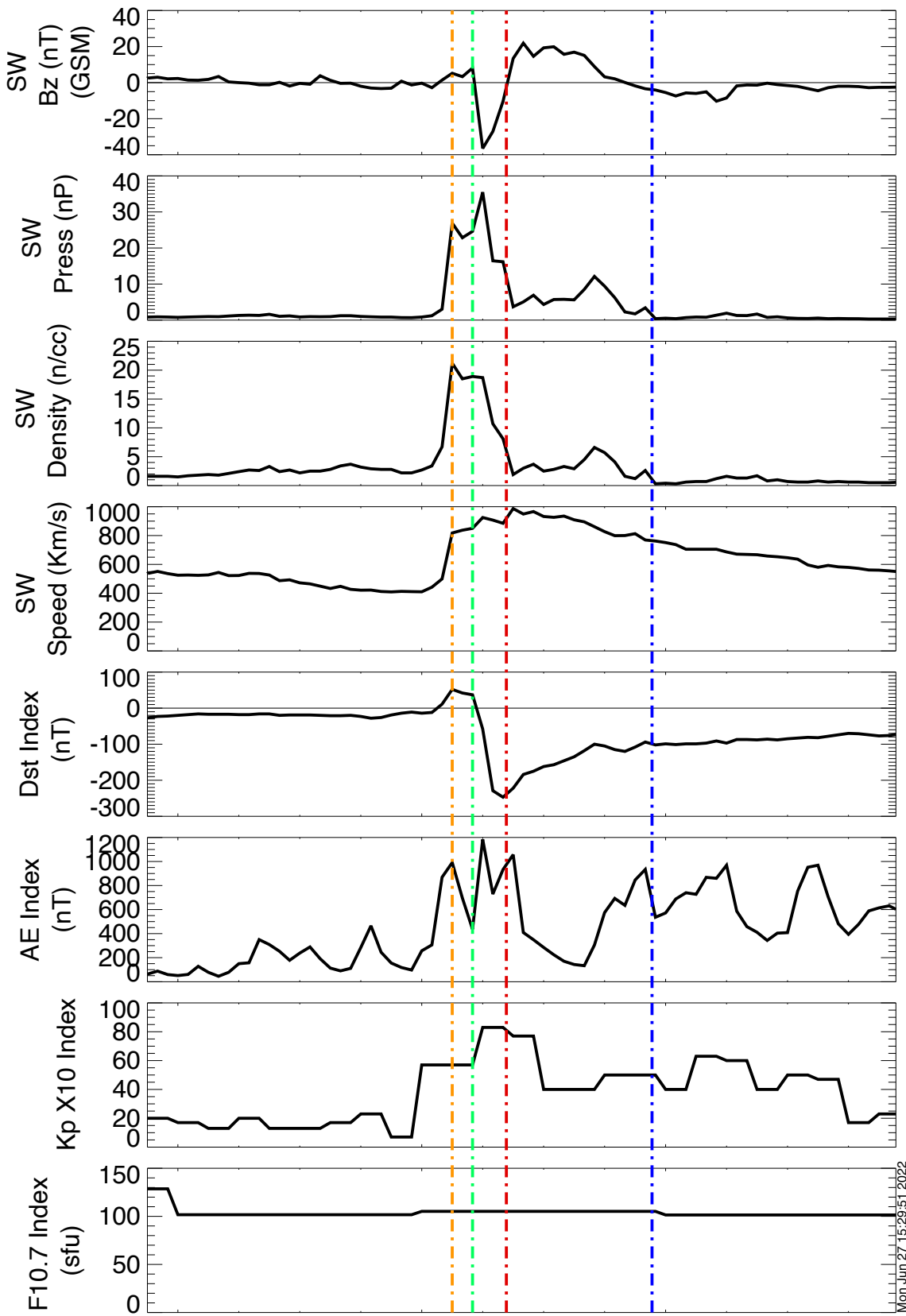


Figure 11. The top and bottom panels present the averaged  $H^+$  and  $O^+$  fluxes from various spacecraft at different altitudes. The fluxes are from the quiet time of minimum phase rows in Table 2.

Figure 1.

2005-05-15/05:00



Mon Jun 27 15:29:51 2022

Date  
2005 May

14

15

16

Figure 2.

# Solar Cycle 23

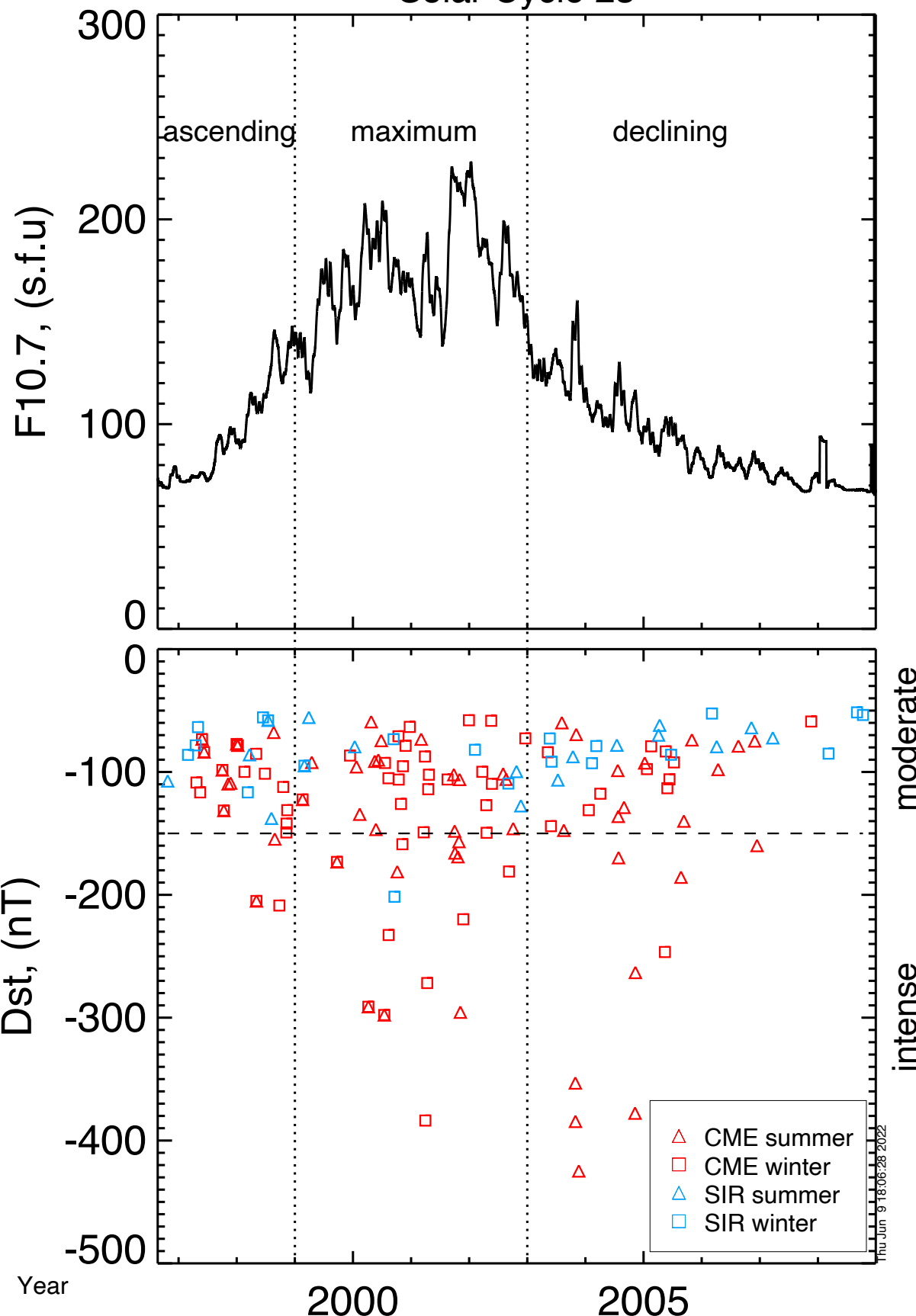


Figure 3.

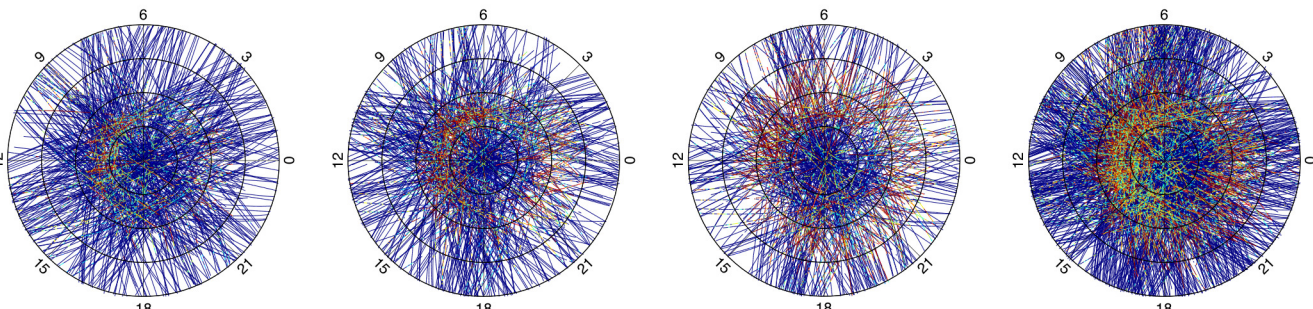


Figure 4.

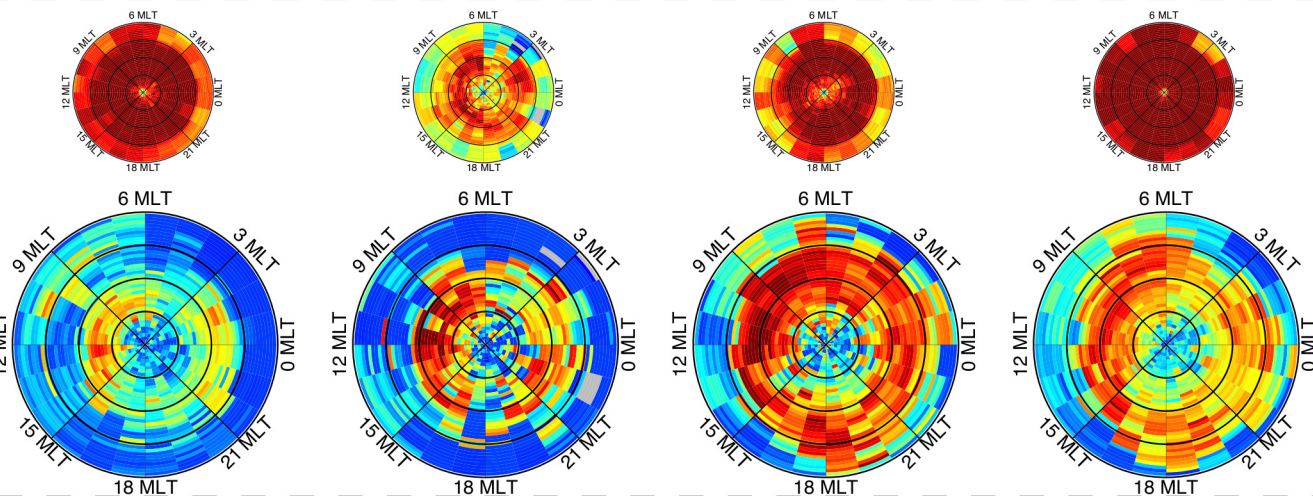
# $O^+$ , CME

pre-storm      initial      main      recovery

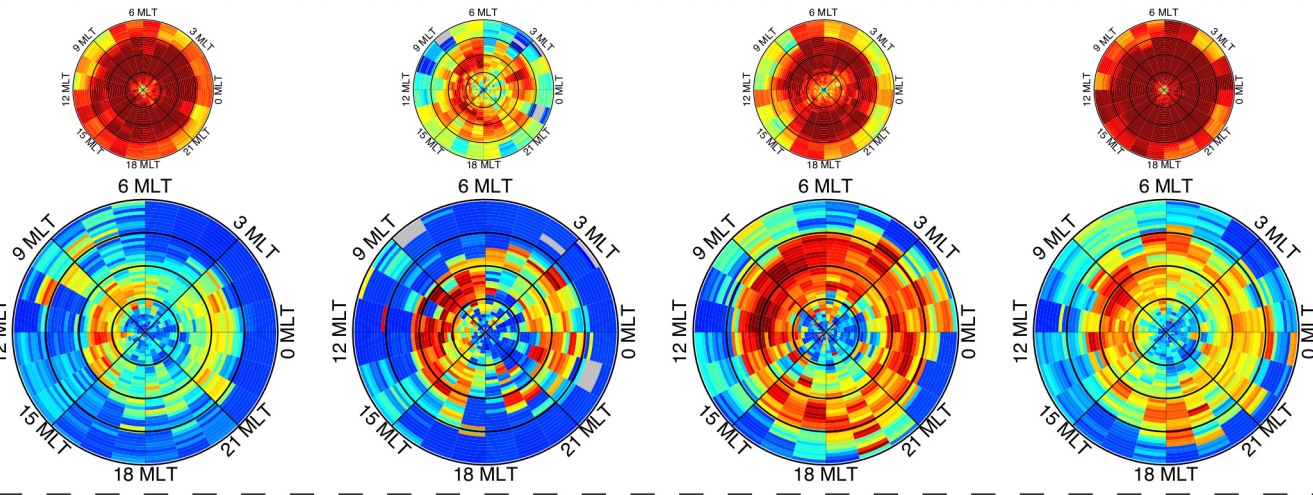
trajectory



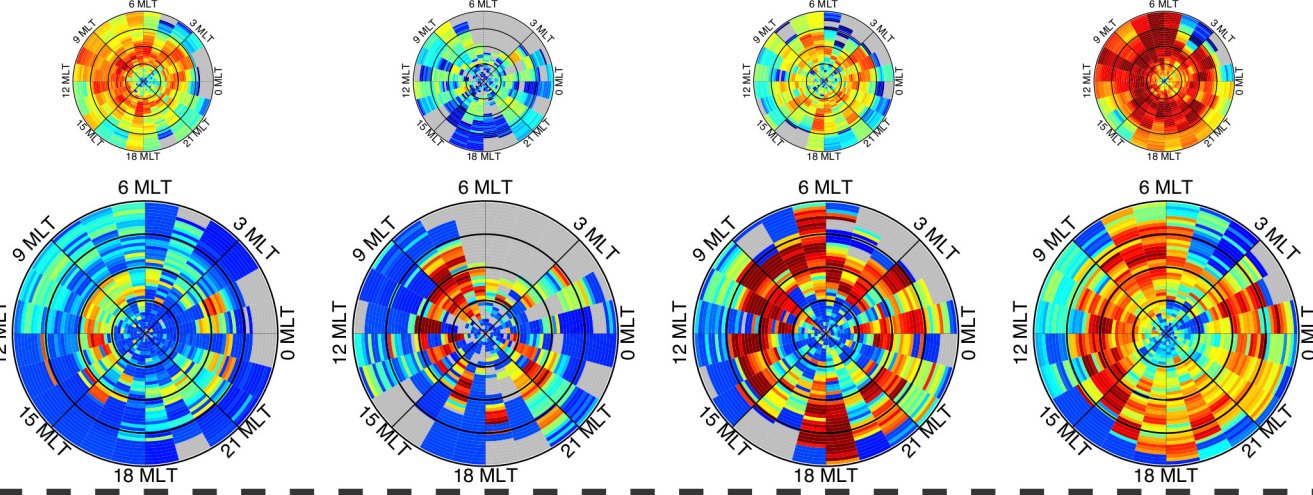
all storms



moderate



intense



Flux( $\text{cm}^{-2} \cdot \text{s}^{-1}$ )

MEAN(flux), ( $\text{cm}^{-2} \cdot \text{s}^{-1}$ )

Figure 5.

# $O^+$ , SIR

pre-storm      initial      main      recovery

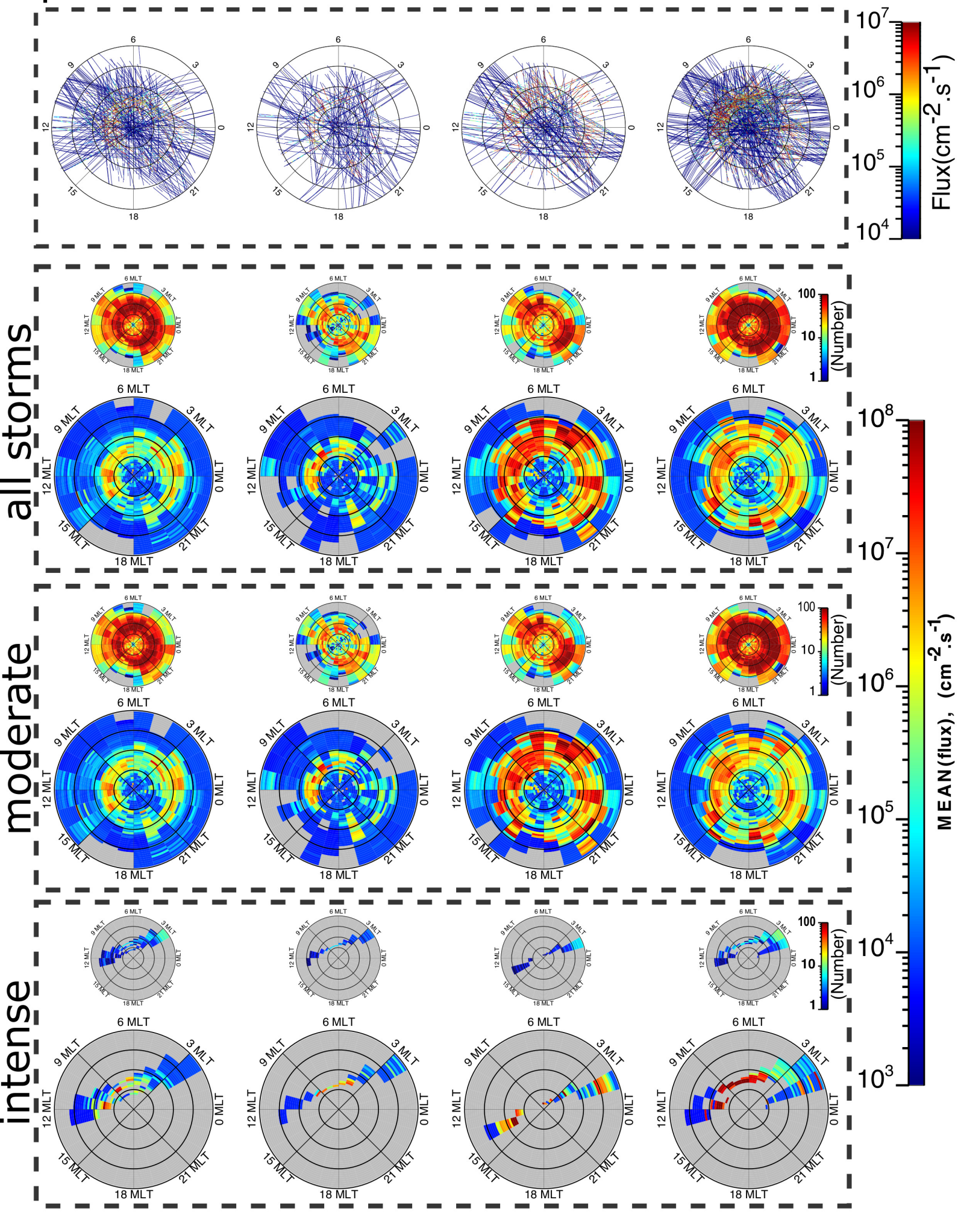


Figure 6.



O<sup>+</sup>

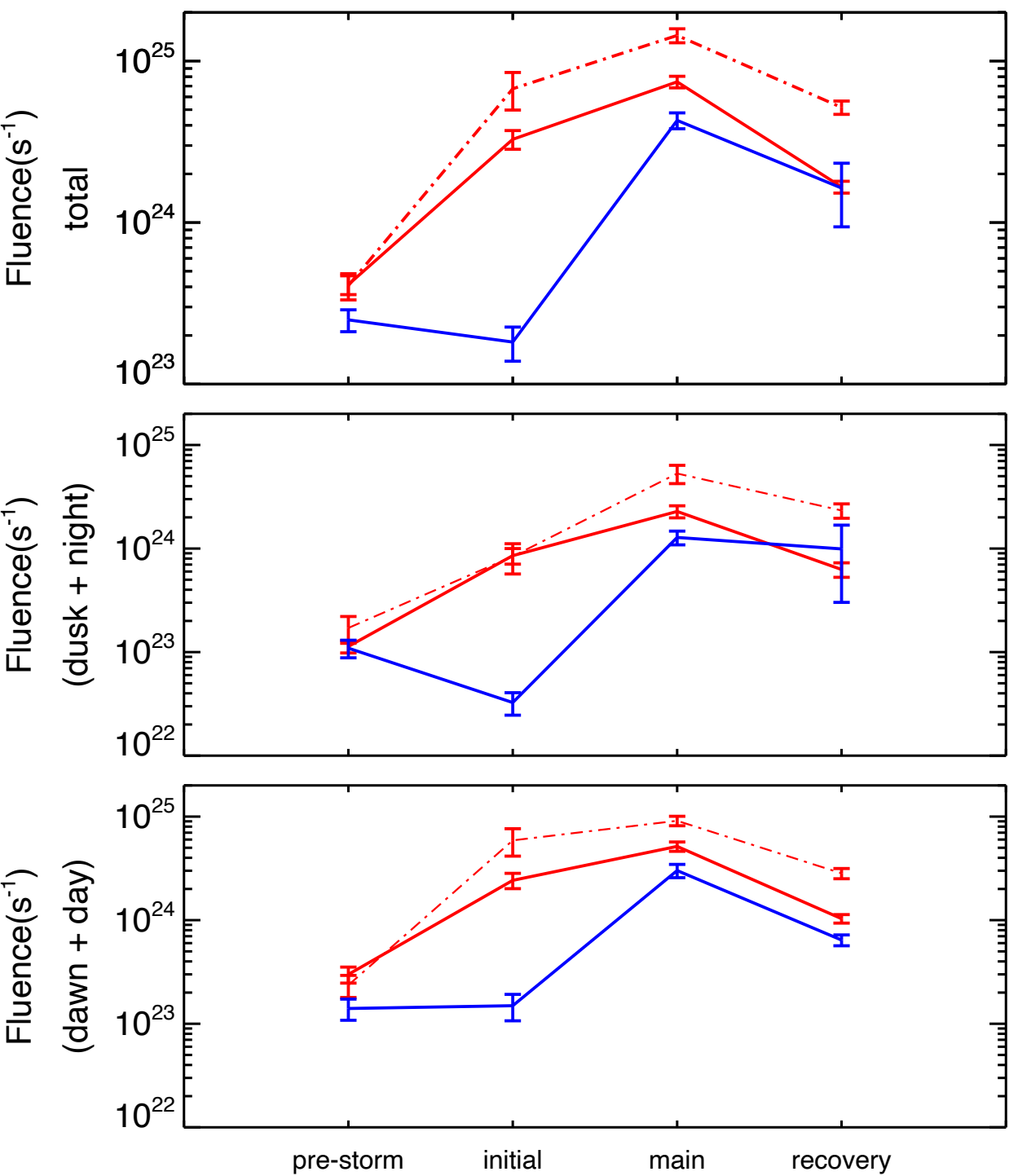
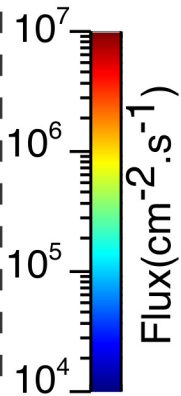
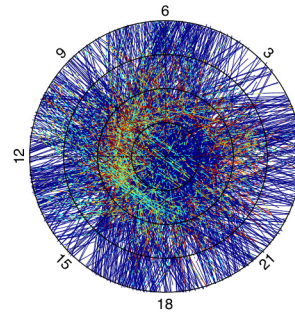
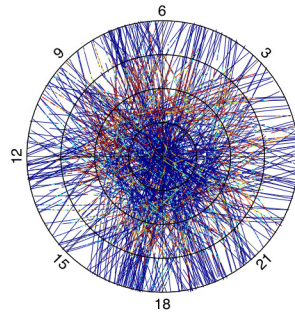
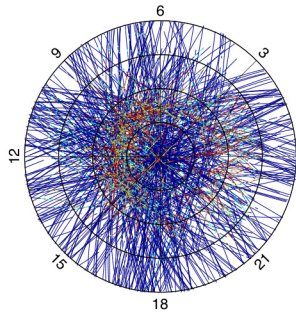
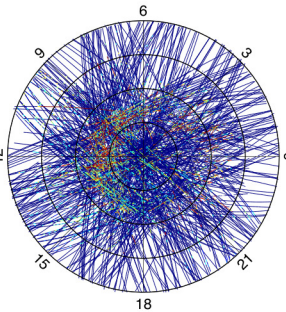


Figure 7.

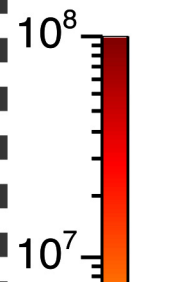
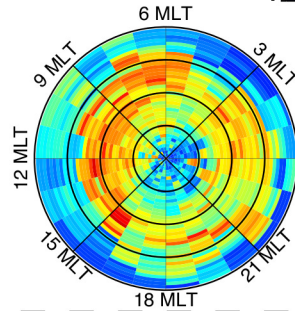
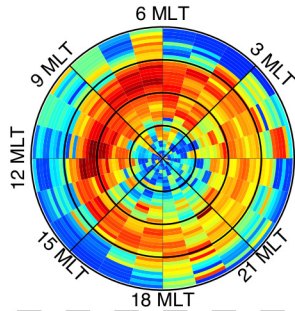
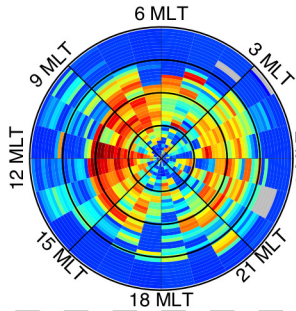
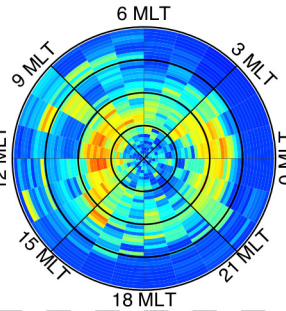
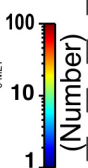
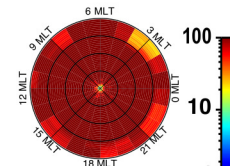
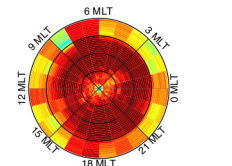
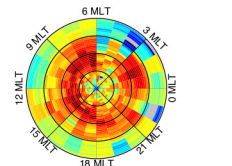
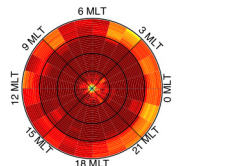
# H<sup>+</sup>, CME

pre-storm      initial      main      recovery

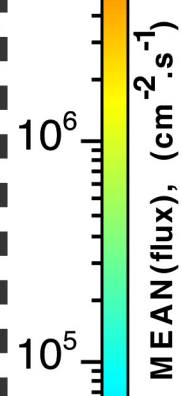
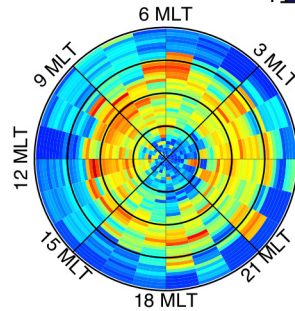
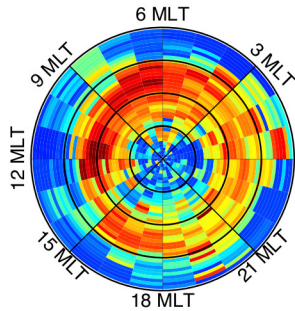
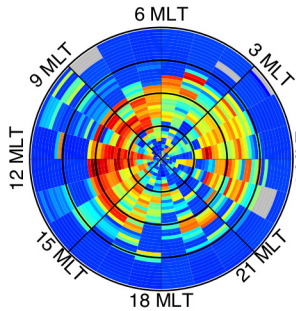
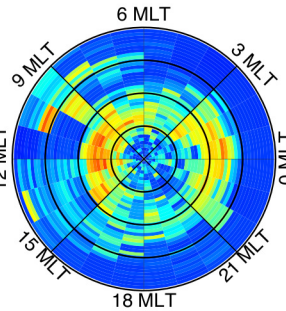
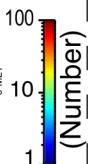
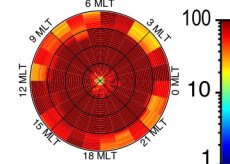
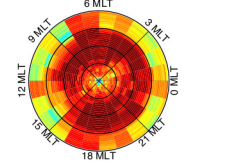
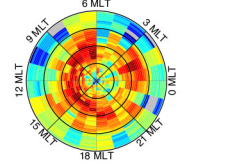
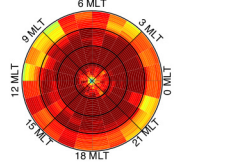
trajectory



all storms



moderate



intense

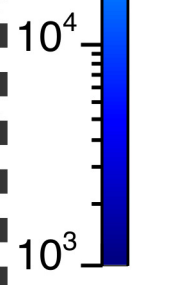
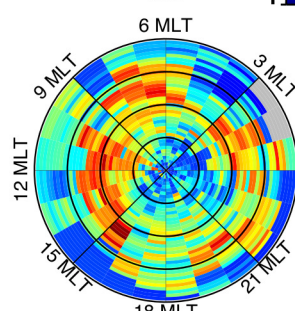
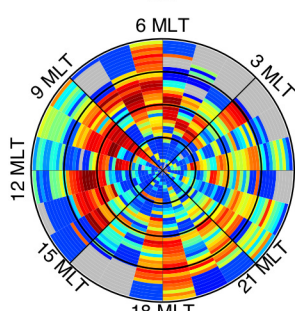
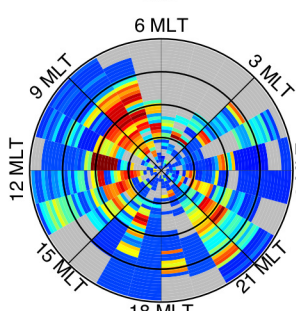
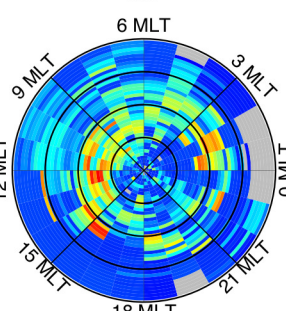
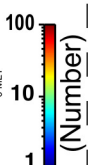
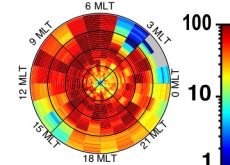
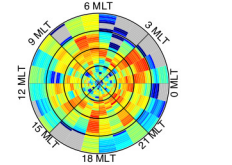
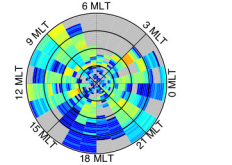
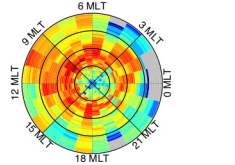
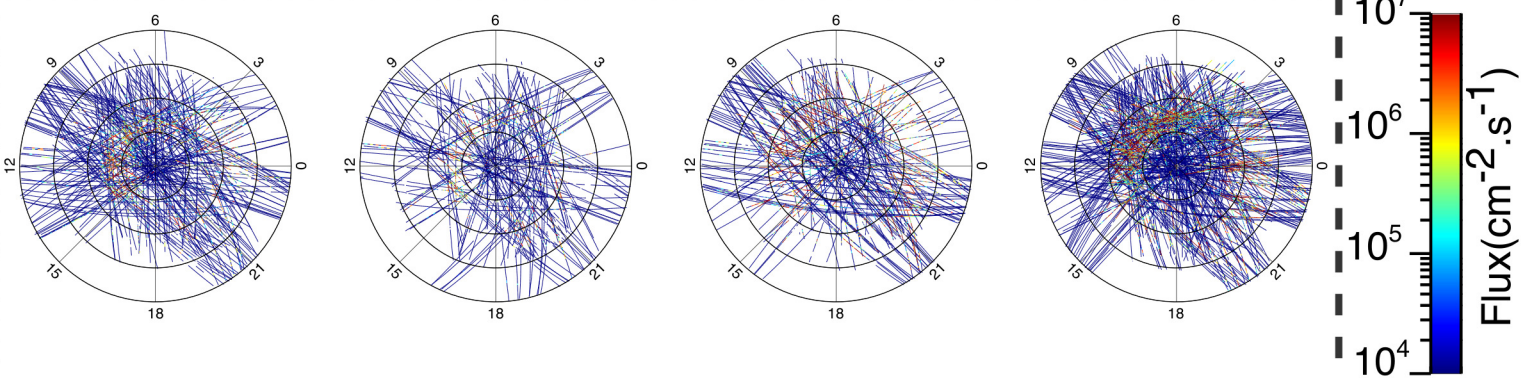


Figure 8.

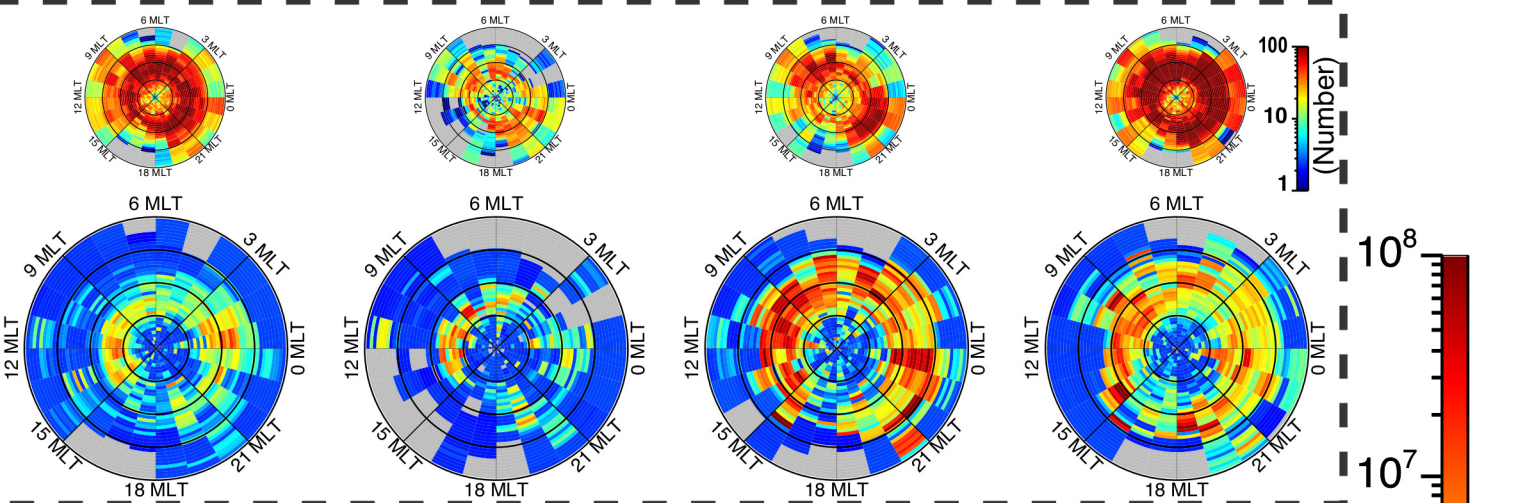
# H<sup>+</sup>, SIR

pre-storm      initial      main      recovery

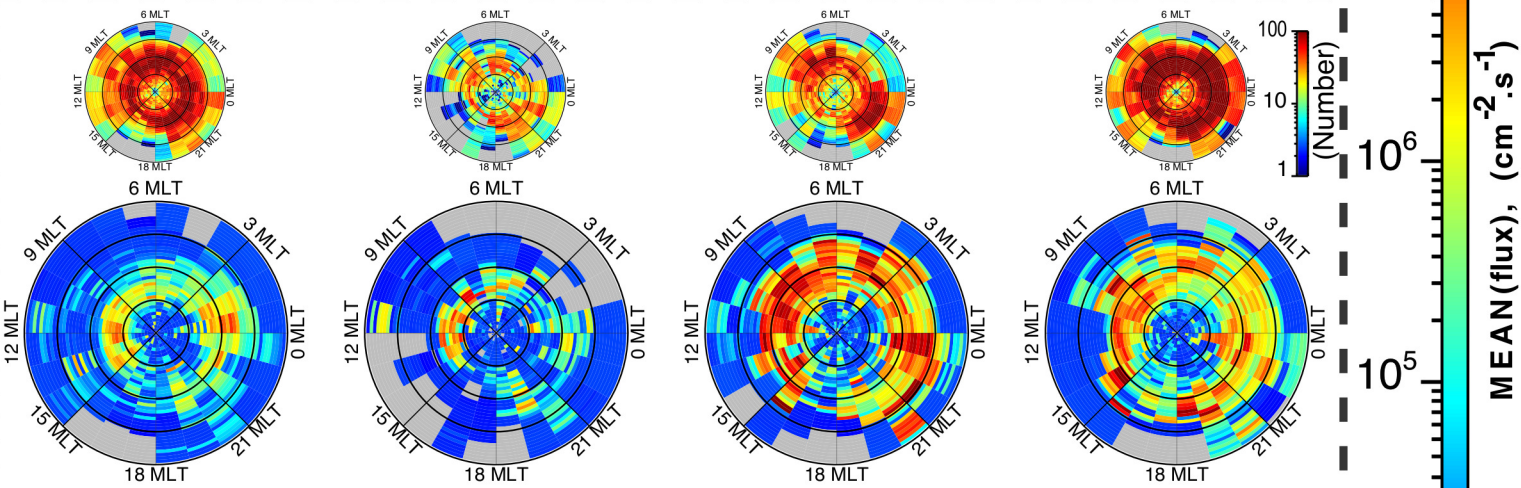
trajectory



all storms



moderate



intense

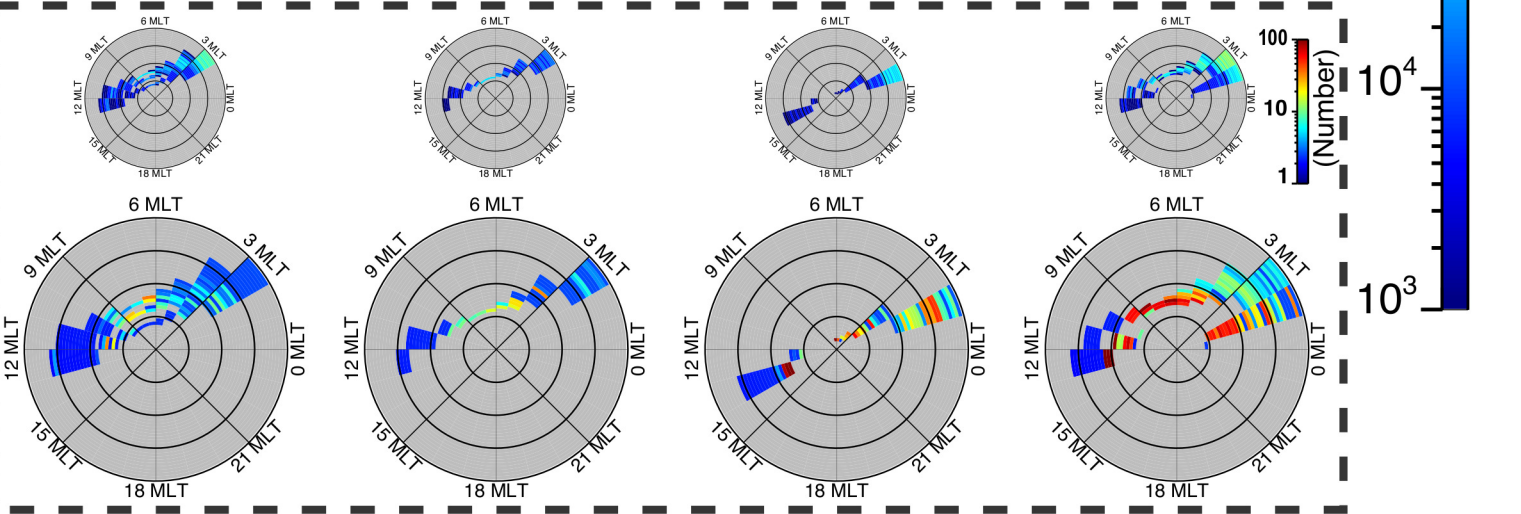


Figure 9.

- CME moderate storms
- - - CME intense storms
- SIR moderate storms

$H^+$

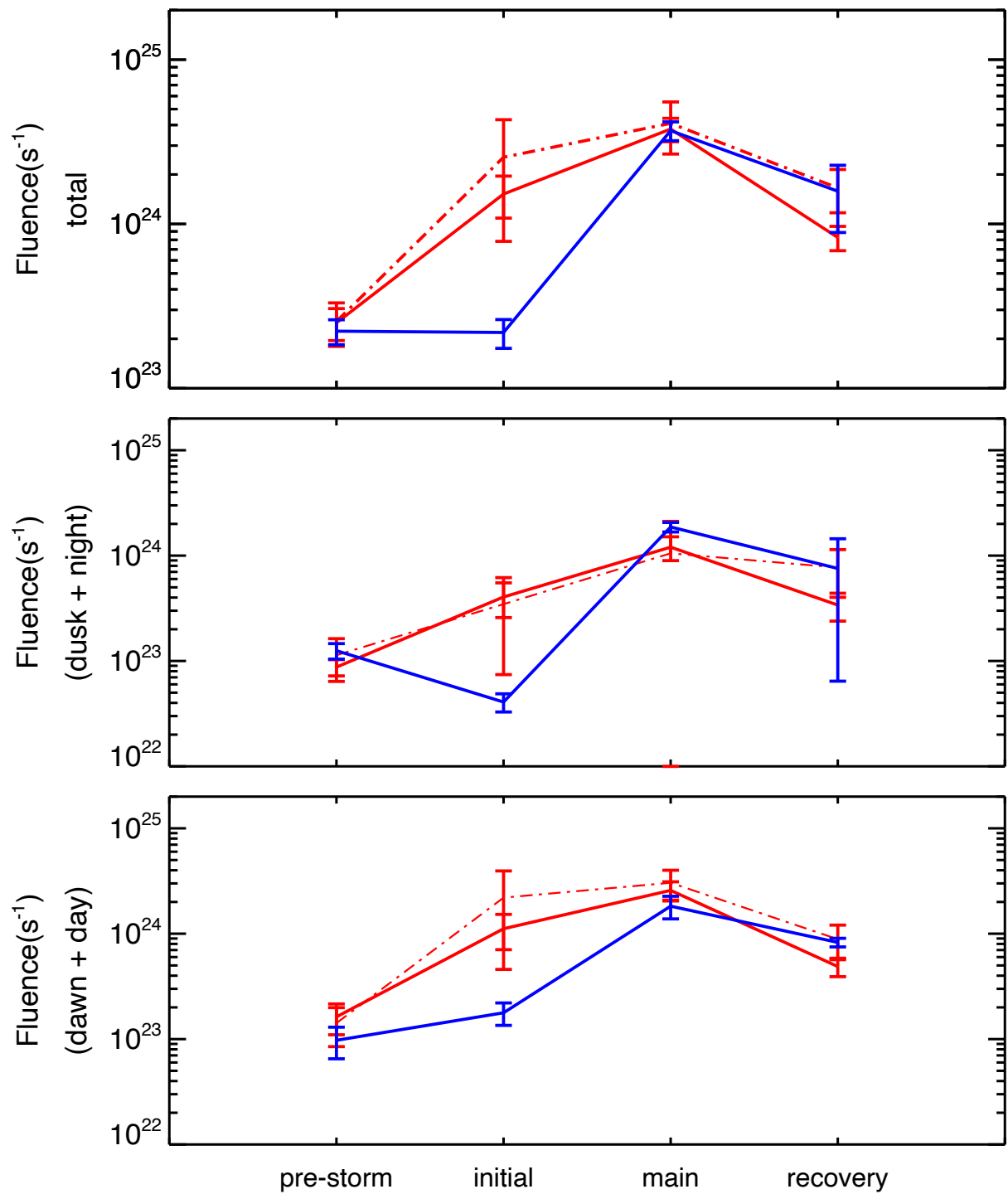


Figure 10.

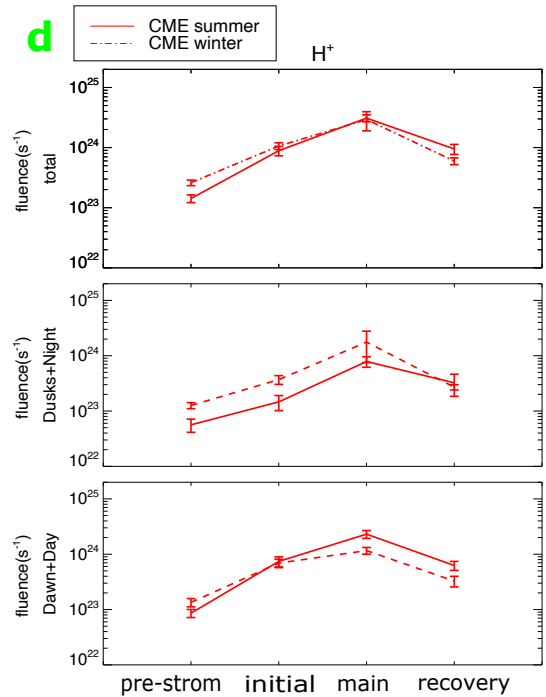
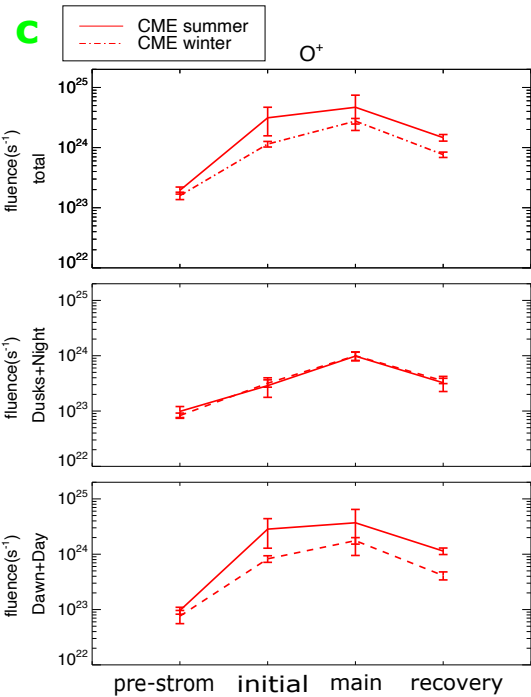
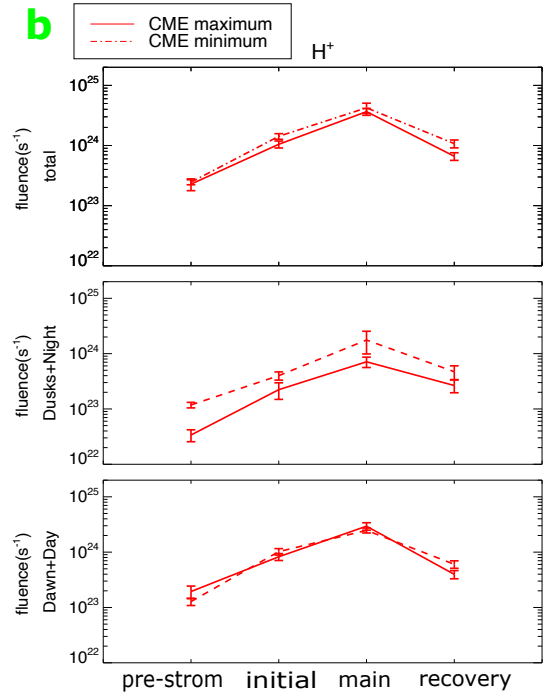
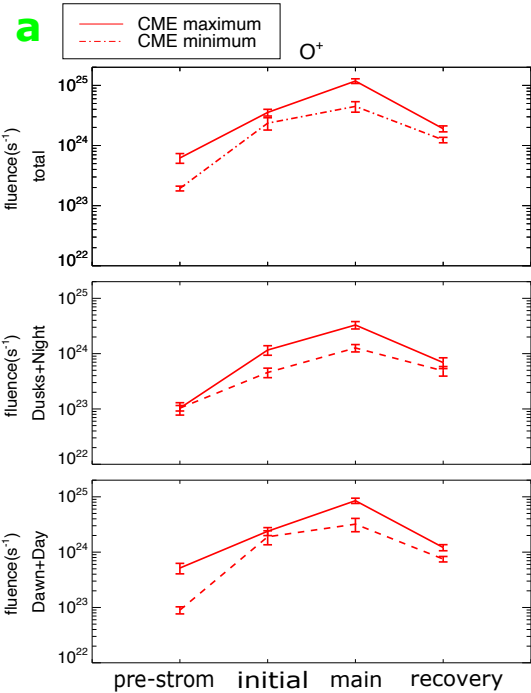


Figure 11.

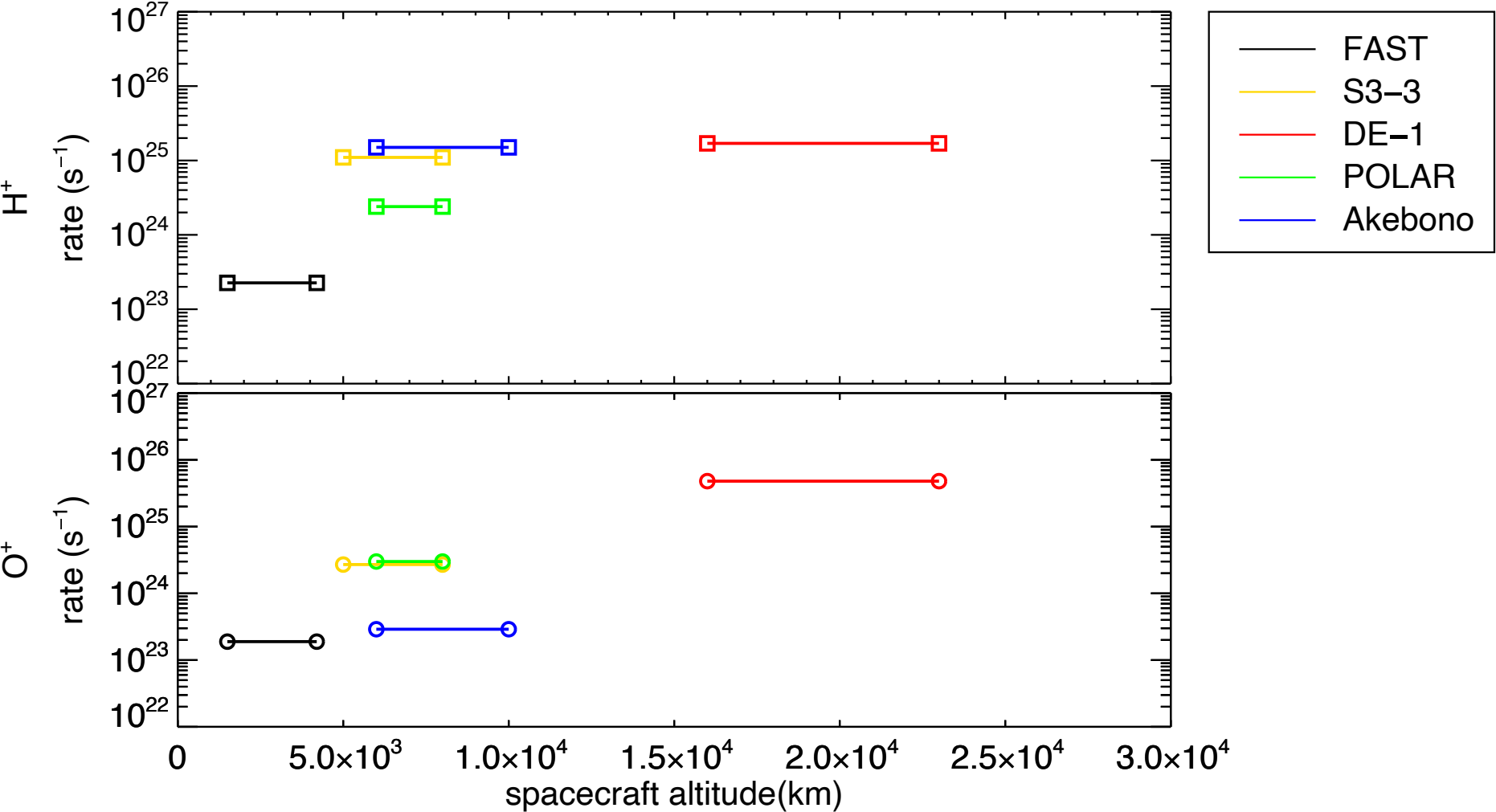


Table 1. Geomagnetic storms with identified drivers from 1996 to 2008.

	<b>TOTAL</b>	<b>CME</b>	<b>SIR</b>
<b>total storms</b>	139	104	35
<b>intense storm(I-storms)</b>	27	26	1
<b>moderate storm(M-storms)</b>	112	78	34
<b>M-storm in maximum phase</b>	45	37	8
		Summer: 15	Summer: 4
		Winter: 21	Winter: 3
		Summer and winter: 1	Summer and winter: 1
<b>M- storm in minimum phase</b>	67	41	26
		Summer: 15	Summer: 11
		Winter: 20	Winter: 14
		Summer and winter: 6	Summer and winter: 1

Table 2. Comparing the total H<sup>+</sup> and O<sup>+</sup> fluences scaping from ionosphere in different studies.

			<b>This Study<sup>1</sup></b>	<b>Collin<sup>2</sup></b>	<b>Yau<sup>3</sup></b>	<b>Peterson<sup>4</sup></b>	<b>Cully<sup>5</sup></b>
<b>Spacecraft</b>			FAST (TEAMS)	S3-3 (Lockheed)	DE-1 (EICS)	Polar (TIMAS)	Akebono (SMS)
<b>Data years</b>			1996-08 to 2009-12	1983-02 to 1984-05	1981-09 to 1984-05	1996-04 to 1998-09	1989-10 to 1998-09
<b>Quiet time</b>			$K_p \leq 3$ and 24 hours before initiating of storms	$K_p \leq 3$ 4-dayas after $Dst > -30nT$	$K_p \leq 2$	$0 \leq K_p \leq 7$ With $\overline{K_p} = 2 -$	$K_p \leq 2$
<b>Active time</b>			three phases of CME and SIR moderate storms	$3 < K_p \leq 5$	$K_p \geq 3$		$K_p \geq 3$
<b>Altitude(km)</b>			1500-4200	5000-8000	16000-23000	6000-8000	6000-10000
<b>Energy(eV/e)</b>			10-12000	500-16000	10-17000	15-33000	1-70
<b>ILAT</b>			$> 50^\circ$	$> 60^\circ$	$> 56^\circ$	$> 55^\circ$	$> 65^\circ$
<b>Data from Hemisphere(s)</b>			North, South	North, South	North, South	South	North
<b>H<sup>+</sup> rate (s<sup>-1</sup>)</b>	<b>Solar maximum</b>	<b>Active</b>	$2.29 \times 10^{24}$		$8.5 \times 10^{25}$		$7 \times 10^{25}$
		<b>Quiet</b>	$2.63 \times 10^{23}$		$2.9 \times 10^{25}$		$3.1 \times 10^{25}$
	<b>Solar minimum</b>	<b>Active</b>	$2.15 \times 10^{24}$	$3.0 \times 10^{25}$	$8.5 \times 10^{25}$		$2.6 \times 10^{25}$
		<b>Quiet</b>	$2.26 \times 10^{23}$	$1.1 \times 10^{25}$	$1.7 \times 10^{25}$	$2.4 \times 10^{24}$	$1.5 \times 10^{25}$
<b>O<sup>+</sup> rate (s<sup>-1</sup>)</b>	<b>Solar maximum</b>	<b>Active</b>	$4.62 \times 10^{24}$		$2.4 \times 10^{26}$		$7.5 \times 10^{25}$
		<b>Quiet</b>	$5.97 \times 10^{23}$		$2.1 \times 10^{25}$		$1.2 \times 10^{25}$
	<b>Solar minimum</b>	<b>Active</b>	$2.15 \times 10^{24}$	$4.2 \times 10^{25}$	$8.85 \times 10^{25}$		$4 \times 10^{24}$
		<b>Quiet</b>	$1.89 \times 10^{23}$	$0.27 \times 10^{25}$	$4.8 \times 10^{25}$	$3 \times 10^{24}$	$2.9 \times 10^{23}$

<sup>1</sup> From observations reported in this paper.

<sup>2</sup> From Table 1. in (Collin et al., 1984).

<sup>3</sup> From Figure 3. in (Yau et al., 1988).

<sup>4</sup> From Table 5. in (Peterson et al., 2001).

<sup>5</sup> From Figure 3. in (Cully et al., 2003)